

Sustainable multigeneration via hybrid biomass-solar energy: Dynamic modeling, thermochemical storage, and green methane production

Arman Adouli^a, Ayat Gharehghani^{a,*}, Jabraeil Ahbab Saray^a, Amirali Shirzad^a, Amin Mahmoudzadeh Andwari^b

^a School of Mechanical Engineering, Iran University of Science and Technology, Tehran, Iran

^b Machine and Vehicle Design (MVD), Materials and Mechanical Engineering, Faculty of Technology, University of Oulu, FI-90014, Oulu, Finland

HIGHLIGHTS

- Dynamic modeling of biomass-solar system for heat, power, and green methane.
- The hybrid system involves sCO₂, S-Graz cycle, and thermochemical CaCO₃/CaO storage.
- 4E and dynamic analysis shows exergy up to 49.87 % and \$44.83M NPV achieved.
- Economics show \$44.83M NPV, 20.53 % IRR, and 6.03 years simple payback period.
- Integration of S-Graz and methanation enables 966.55 kg/h green methane production.

ARTICLE INFO

Keywords:
S-Graz cycle
Thermochemical energy storage
Methanation
Heliostat field
Dynamic modeling

ABSTRACT

This paper presents the conceptual design, dynamic modelling, and comprehensive performance analysis of a novel biomass-solar hybrid multigeneration system producing heating, electricity, and green methane. This system integrates advanced thermodynamic components, including a supercritical CO₂ cycle, the S-Graz power cycle, a heliostat field, and a thermochemical energy storage subsystem utilizing the reversible CaCO₃/CaO reaction. To enable continuous 24-h operation, the system is configured in two distinct modes: a solar-driven daytime mode and a nighttime mode powered by stored thermal energy. A PEM electrolyzer and a methanation reactor are incorporated to convert captured CO₂ and produce hydrogen into green methane, promoting carbon circularity. A thorough 4E (energy, exergy, economic, and environmental) analysis is conducted alongside a detailed parametric and dynamic investigation across seasonal and hourly variations. Two different scenarios regarding methane generation are also considered and compared. Economic analysis yields a net present value of \$44.83 million, an internal rate of return of 20.53 %, and a levelized cost of electricity of 8.01 cents/kWh, with a simple payback period of 6.03 years. Sensitivity analyses reveal that solar irradiance, biomass feed rate, and thermochemical heat storage ratios significantly impact overall system performance. The proposed hybrid system demonstrates a viable pathway for low-emission, multi-output energy production by integrating renewable resources with innovative carbon reuse technologies.

1. Introduction

1.1. Pressing global challenges

Climate change, driven by the extensive burning of fossil fuels, has become one of the most pressing global challenges of our time (Hossein Fakhri et al., 2024). The resulting greenhouse gas emissions, particularly CO₂, have resulted in escalating global temperatures, more

frequent and intense weather events, and significant ecological disruptions (Abifarin et al., 2025) (Abifarin et al., 2024a). To alleviate these effects, it is imperative to accelerate the shift from carbon-based fuels to sustainable energy alternatives that are sustainable, abundant, and environmentally friendly (Mehrenjani et al., 2024) (Farahmandfar et al., 2025).

Among these, biomass stands out as a highly promising source of renewable energy given its accessibility, carbon neutrality, and ability to

* Corresponding author.

E-mail address: ayat_gharehghani@iust.ac.ir (A. Gharehghani).

Table 1

Some cases regarding systems powered by solar/biomass energy sources.

References	Power source		Analysis		Outputs		
	Biomass	Solar	4E	Dynamic	Power	Heating	E-fuels
Saleh Kandezi and Mousavi Naeenian (2022)	-	✓	-	✓	✓	✓	-
Boukelia et al. (2025)	-	✓	-	-	✓	-	✓
Yao and Wu (2025)	✓	-	✓	-	✓	-	✓
Zhang and Sobhani (2024)	✓	-	-	-	✓	✓	-
Wang et al. (2023)	✓	-	✓	-	✓	✓	-
Zhang et al. (2023)	✓	-	-	-	✓	✓	-
Wang et al. (2025)	-	✓	-	-	✓	-	✓
This study	✓	✓	✓	✓	✓	✓	✓

utilize organic waste materials (Abifar and Abifar, 2024). Biomass is converted into energy by going through a number of processes, including combustion, anaerobic digestion, and gasification, making it a versatile option to reduce reliance on traditional fossil fuels. Additionally, the integration of other renewable sources of energy with biomass, namely solar energy, can further enhance its potential.

A key challenge in the renewable energy transition is the production of sustainable biofuels, such as methane, which can serve as a clean alternative to fossil fuels. Methane offers several privileges, such as high energy density and compatibility with existing natural gas infrastructure. Producing green methane through near-zero emission processes is critical to achieving decarbonization goals. Syngas, a mix of carbon monoxide and hydrogen made from the gasification of biomass, holds significant potential for conversion into biofuels, including methane. However, the methanation process requires a reliable source of hydrogen. Proton exchange membrane (PEM) electrolyzers have emerged as an ideal solution for hydrogen production owing to their stability, notable efficiency, scalability, and operability using renewable electricity, such as solar or wind power. Recent studies focusing on biomass as a renewable source of energy in order to move towards a sustainable future are discussed in the following.

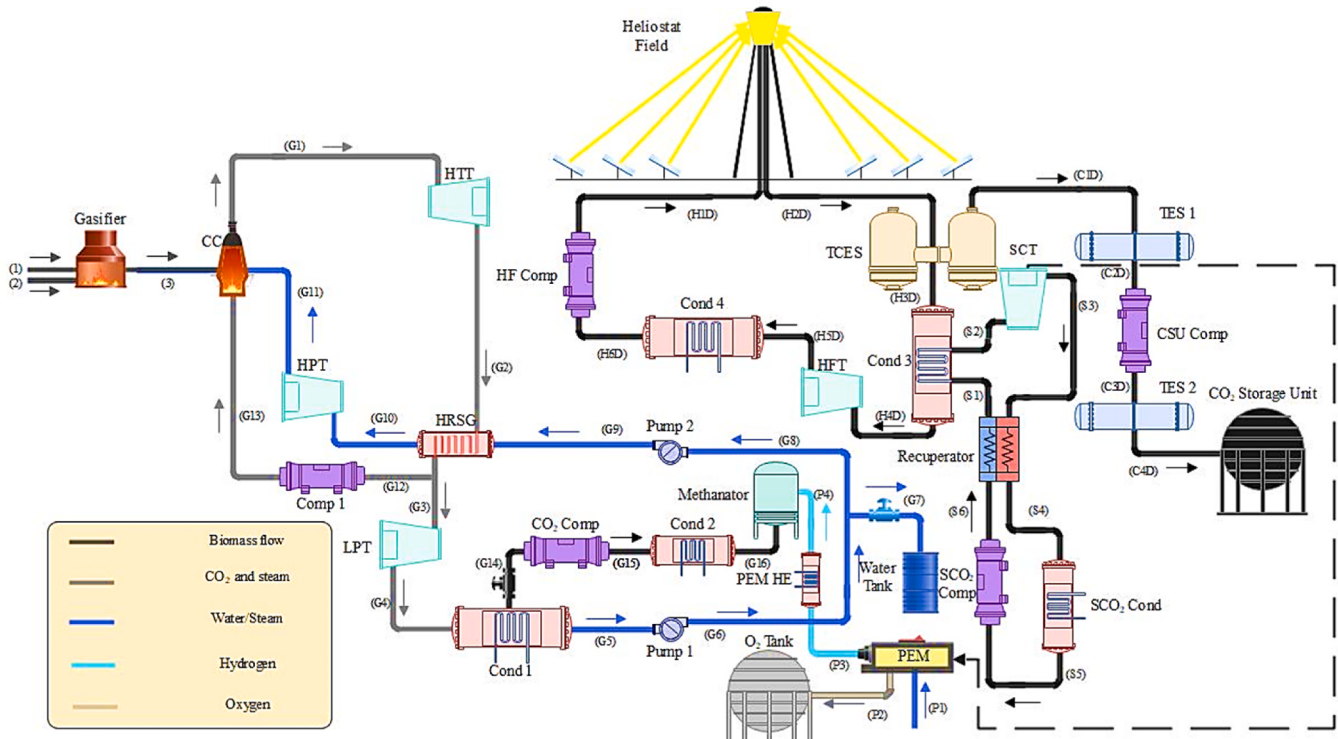
1.2. Literature review

Shokri et al. (2024) developed a biomass-driven polygeneration system producing heating, electricity, hydrogen, and freshwater, achieving 67.7 % efficiency and 22.3 kg/h hydrogen output. Using municipal solid waste and CO₂, energy cost was 11.4 \$/GJ. Abedinia et al. (2024) proposed a system integrating Kalina cycle, syngas-fueled SOFC, PEM electrolyzer and desalination, achieving 53.7 % energy and 38.2 % exergy efficiency and a 4-year payback period. Wang et al. (2024) developed a renewable energy system integrating biomass gasification, PEM electrolysis, geothermal energy, thermoelectric generators, and HDH desalination. Optimization achieved 47.9 % exergy efficiency, 5958 kW power, and 56.9 \$/GJ product cost, producing 56.1 kg/h hydrogen. Zhang et al. (Zhang and Sobhani, 2024) designed a biomass-based integrated system producing heating, power, cooling, and potable water using a biogas digester, gas turbine cycle, supercritical CO₂ cycle, and reverse osmosis unit. Optimized via particle swarm optimization, it achieved 38.5 % exergy efficiency, 41112 kW power, 1384 kW cooling, 28414 kW heating, 18.7 \$/GJ product cost, and \$75.2 million net present value. Kamari et al. (Lak Kamari et al., 2023) developed a biomass-fueled system for district heating, cooling, bioethanol, biogas, and electricity. Evaluating 15 biomass sources, they found cotton stem had the highest amount of CO₂ emissions (195 kg/MWh) and switchgrass had the lowest (147 kg/MWh). Rice straw caused the highest (45.3 %) and larch wood caused the lowest (42.9 %) exergy efficiency. The burner had the highest amount of exergy destruction. Wang et al. (2023) introduced a multi-criteria analysis method for a polygeneration cycle integrating a biomass syngas-fueled SOFC, gas turbine, thermoelectric generator, and absorption chiller.

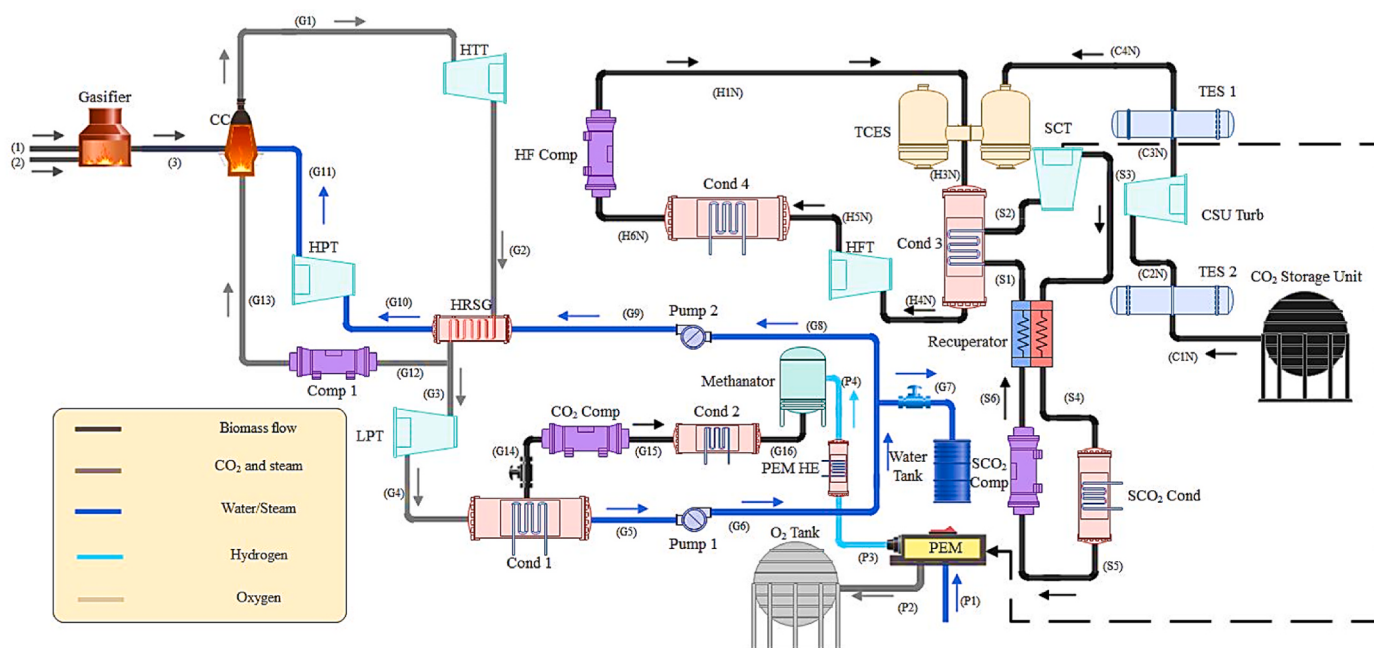
The system recycled CO₂ and synthesized methane, reducing emissions. Genetic algorithm optimization showed competitive efficiency, cost, and environmental sustainability.

Solar and biomass energy integration in multigeneration systems has emerged as a key advancement in renewable energy. These hybrid systems improve efficiencies and mitigate environmental impact by producing multiple valuable outputs, including heating, cooling, power, hydrogen, and other synthesized products. Sharifishourabi et al. (2024) developed a biomass-solar polygeneration system integrating thermodynamic cycles and hydrogen production, achieving exergy and energy efficiencies of 71.25 % and 37.68 %, respectively. Their economic assessment revealed that at an initial cost of \$53.8 million, net present value could range from 6.87 up to 173.4 million dollars by 2054, depending on hydrogen prices fluctuating between \$7000 and \$13,000 per ton. Sabbaghi et al. (2024) designed a polygeneration system combining biomass and solar energy sources with five integrated cycles, including a trans-critical CO₂ cycle, a gas turbine, and Rankine cycle. Their system, which incorporated a proton exchange membrane electrolyzer for the production of hydrogen, gained exergy and energy efficiencies of 15.2 % and 20.2 %, respectively, with a cost rate of 0.007554 \$/s and an environmental impact rate of 0.0008611 pt/s. Altayib et al. (Altayib and Dincer, 2024) designed a large-scale biomass-solar-based system for Al Lith, Saudi Arabia, achieving 53 % energy and 45 % exergy efficiencies. Their system demonstrated impressive annual production figures, including 1036 GWh of power, 858 GWh of heat, 23 GWh of cooling, 11,300 tons of ammonia, 1800 tons of urea, 113,000 tons of sodium hydroxide, and 905,000 m³ of freshwater. They optimized biomass oxy-gasifier parameters, selecting an oxygen-to-biomass proportion of 0.15 and a steam-to-biomass proportion of 0.1. Yang et al. (2024) designed a solar-biomass-based combined power, cooling, and heating system with an organic Rankine cycle, analyzing its performance. Their results showed unit exergy costs between 2.742 and 27.1 MW/MW and exergoeconomic costs ranging from 41.11 to 507.1 \$/MWh, emphasizing the importance of optimizing solar collector efficiency and key components to enhance sustainability and reduce environmental impact.

Capturing CO₂ in integrated energy systems is crucial for mitigating climate change by reducing emissions from power generation and industry. Research focuses on advancing carbon capture and utilization (CCU) technologies, optimizing renewable energy integration, and improving cost-effectiveness. Zhang et al. (2023) designed a system integrating power, cooling, heating, and dehumidification using gasification of food waste plasma and solid oxide fuel cells (SOFC). It achieved net exergy, thermal and electrical efficiencies of 51.15 %, 84.22 %, and 54.60 %, respectively, with a CO₂ removal rate of 97.17 %. Safder et al. (2024) introduced a near-zero CO₂ emission multigeneration system using biomass gasification, producing 190 kg/h of H₂ and 430.25 kg/h of methanol, with exergy and energy efficiencies of 71.63 % and 78.13 %, reducing CO₂ emissions by 78.5 %. Jasim et al. (Jasim et al., 2024) developed a polygeneration system with a CO₂ separation and liquefaction cycle, producing 42.72 MW of power, 612 kmol/h of liquefied



(a)



(b)

Fig. 1. The schematics of the system operating during a) daytime and b) nighttime.

CO_2 , and 18010 kmol/h of natural gas,. The system's exergy and energy efficiencies reached 87.72 % and 32.08 %, with CO_2 and electricity costs of 0.0728 \$/kg and 0.0466 \$/kWh. [Zhang et al. \(2025a\)](#) modified the Allam cycle, achieving 41.22 % energy efficiency and 57 % exergy efficiency with zero CO_2 emissions. The system converted CO_2 into

methane via electroreduction, demonstrating potential for sustainable energy production.

Table 1 provides an overview of the most influential recent investigations into multigeneration systems powered by solar and/or biomass, detailing their configurations, output streams (electricity, heat,

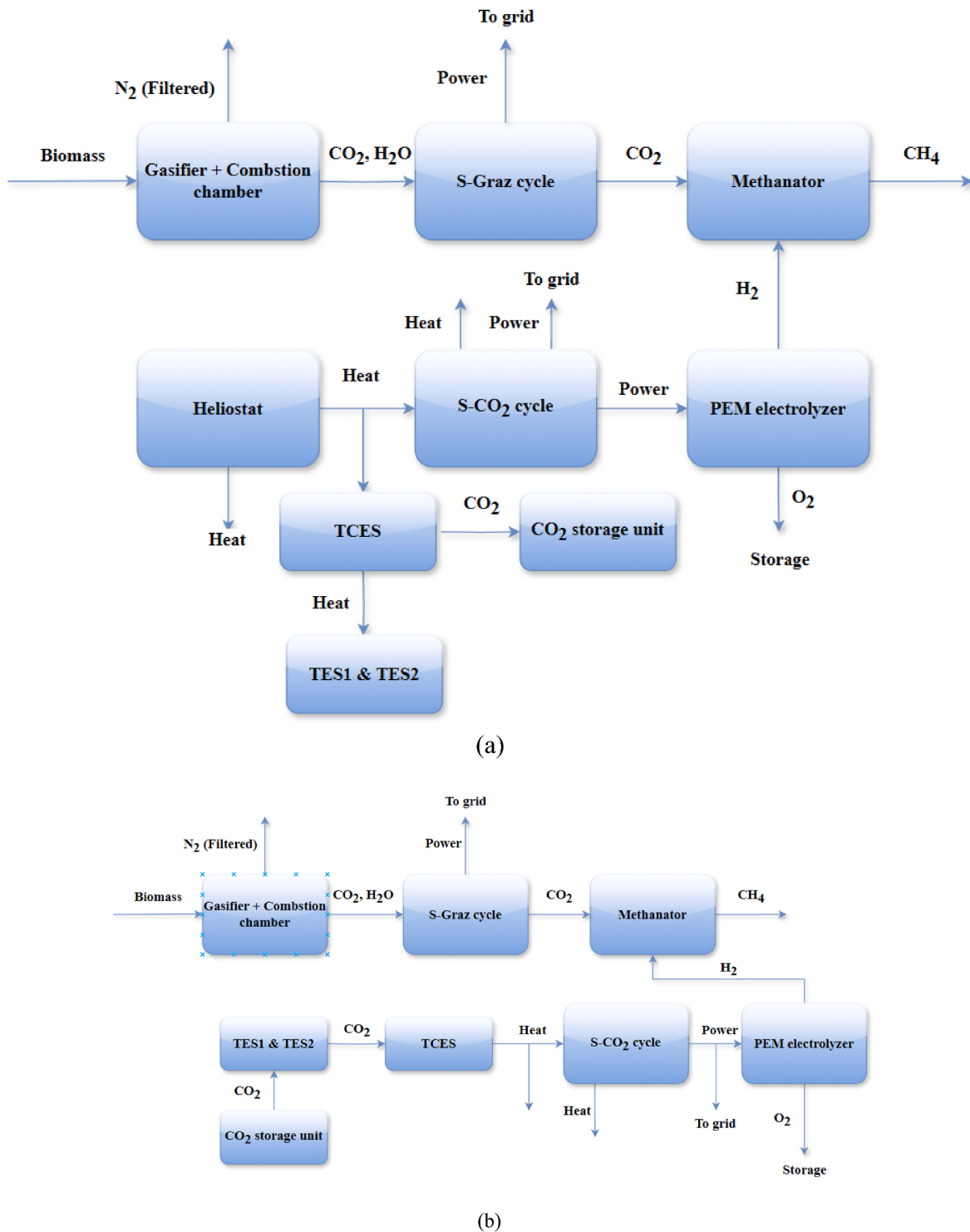


Fig. 2. Flowchart of mass and energy flow during a) daytime operation and b) nighttime operation.

hydrogen, desalinated water, etc.), and the scope of their performance analyses. While these studies offer valuable insights into static performance metrics and parametric sensitivities, they seldom track how system outputs evolve dynamically over the course of a year or within daily solar cycles. To address this gap, this study proposes a novel system that leverages both solar irradiation and biomass feedstock, and undertakes a truly dynamic assessment—examining seasonal variations and hourly operational profiles.

Another key contribution of this research is the proposal of a system capable of near-complete CO₂ capture. For this purpose, the design

employs the S-Graz cycle, an advanced oxy-fuel combustion loop that achieves near-complete CO₂ capture within the power block yet has received scant attention in the literature. This cycle is coupled to a heliostat field for concentrated solar input, enabling co-generation of electricity, process heat, and green methane. To address solar intermittency, this system integrates a calcium-looping thermochemical storage subsystem that uses solar heat for daytime endothermic decomposition of CaCO₃ and nocturnal exothermic reformation of it, delivering high-density, long-duration thermal energy. The main highlights and contributions of this work include:

- Hybrid solar-biomass multigeneration architecture: Design and simulation of a system combining biomass gasification with concentrated solar power, featuring the innovative S-Graz cycle to combust syngas in pure oxygen, condense and recycle CO₂, and produce green methane in a closed-loop carbon economy.
- calcium-looping thermochemical storage for nighttime operation: The implementation of a two-reactor CaCO₃/CaO storage cycle to absorb excess solar heat during daylight and release it at night, enabling continuous power and heat output despite the diurnal absence of sunlight.
- Integrated 4E performance evaluation: A full energy, exergy, economic, and environmental analysis which quantifies thermodynamic efficiencies, levelized costs, payback period, and CO₂ savings, providing a holistic view of system viability under realistic cost and resource assumptions.
- Comprehensive dynamic modeling: Performing a month-by-month and hour-by-hour simulation of system behavior—capturing fluctuations in direct normal irradiance, storage charge/discharge cycles, and operational transitions—to reveal performance trends and pinpoint optimal operating strategies across varying climatic conditions.

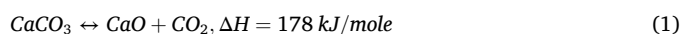
2. System description

The integrated system, as depicted in Fig. 1, comprises six main sections: the gasification unit, The S-Graz cycle, a heliostat field, a supercritical CO₂ (S-CO₂) cycle, a thermochemical energy storage (TCES) subsystem, and a CO₂ storage unit. The S-Graz cycle runs on biomass energy, while the rest of the system is powered by solar energy during daytime and by TCES during nighttime. The energy and mass flow flowcharts of the system modes are illustrated in Fig. 2. A more detailed explanation of each section follows. Several key assumptions have been made in the system's modeling (Yan et al., 2025) (Sun et al., 2024).

- The analysis is conducted assuming the system is in a steady state.
- Effects related to potential and kinetic energy, as well as exergy, are considered insignificant.
- Pressure losses in pipelines and thermal losses occurring in both heat exchangers and piping are disregarded.
- Heat dissipation from storage units containing CaO and solid materials (CaCO₃/CaO) is assumed to be insignificant.
- The plant operates in two distinct modes: a daytime mode, where solar energy is available and stored via TCES, and a nighttime mode, during which TCES serves as the sole energy source.

2.1. TCES system

In the proposed TCES system, CO₂ released during the daytime calcination of calcium carbonate is stored separately from the resulting calcium oxide. At night, these reactants are introduced into the carbonator, where they recombine exothermically to regenerate calcium carbonate, releasing thermal energy that is harnessed for power generation (Alovisio et al., 2017). The reaction is described in Eq. (1):



The carbonator and calciner operate at 8 bar and 1 bar, respectively, with optimal reaction temperatures of 950 °C and 1000 °C determined based on equilibrium considerations. While the decomposition reaction proceeds fully, carbonation is inherently incomplete due to the gradual sintering of CaO particles, which reduces their reactivity over time. As a result, only a fraction of the CaO is converted in each cycle. In line with previous studies, a conservative steady-state conversion ratio of 15 % is assumed in this analysis (Ortiz et al., 2021) (Ortiz et al., 2019).

Recent advancements in thermochemical energy storage enhance solar energy utilization in systems like our S-Graz cycle by enabling

efficient, high-density storage. Innovations in carbonate looping achieve enhanced thermal efficiency with improved particle durability for solar-driven cycles. Hybrid sorbent materials, combining metal oxides with porous supports, offer high storage capacity for low-temperature applications, though long-term material stability remains a challenge (Xu et al., 2025).

2.2. CO₂ storage unit

In the proposed system, CO₂ released from the calciner during daytime operation is temporarily stored and later utilized in the carbonator during nighttime. Upon exiting the TCES at 950 °C, the CO₂ first goes through a high-temperature thermal energy storage (TES1) unit, which in this study uses iron slag as the storage medium due to its favorable thermal retention properties. The gas is then compressed until it reaches 75 bar, then cooled down to 25 °C in a secondary thermal energy storage (TES2) unit, and stored under pressure to minimize volume requirements (Bauer et al., 2012). During nighttime discharge, the stored CO₂ is heated in TES2 and expanded inside a turbine to retrieve a portion of the compression energy, then passes through TES1, where it absorbs additional heat before entering the carbonator. This integrated thermal management strategy allows the system to recover and utilize residual heat effectively, improving its round-the-clock performance (Ortiz et al., 2021) (Ortiz et al., 2019).

2.3. S-CO₂ cycle

Carbon dioxide's critical point, lies near ambient conditions, making it well-suited for supercritical power cycles that can be integrated with conventional cooling technologies. Its favorable thermophysical properties, as highlighted in prior studies, enable high efficiency and flexibility in both stand-alone and hybrid energy systems. In this study, a simple recuperative S-CO₂ cycle is employed to utilize solar heat during daytime operation and thermochemical energy from the carbonation reaction during nighttime operation. During daytime operation, the heliostat working fluid absorbs solar energy and delivers a portion of this energy to the TCES system before entering the power cycle's main heat exchanger. At night, heat is drawn from the exothermic carbonation reaction to drive the same cycle. The selected cycle configuration prioritizes simplicity: CO₂ is compressed, heated in a heat exchanger, expanded inside a turbine in order to generate electrical power, and then partially recuperated before being cooled and recompressed, enabling efficient and continuous operation (Manente and Lazzaretto, 2014).

2.4. S-Graz cycle

The S-Graz Cycle is a high-efficiency, net-zero-emission power generation system that employs oxy-fuel combustion of syngas with pure oxygen, resulting in a flue gas of CO₂ and steam. This high-temperature gas mixture drives a turbine to produce power, after which the energy in the exhaust gas is recovered via a secondary low-temperature Rankine cycle. By coupling gas and steam cycles, the system achieves overall thermal efficiencies of up to 70 %, while also enabling integrated carbon capture. The CO₂ in the exhaust is condensed and separated from water, allowing it to be reused for synthetic fuel production—such as methane—or stored for long-term sequestration, enhancing both the system's environmental and energy performance (Nami et al., 2019).

2.5. PEM electrolyzer

In an electrolysis cell, electrical and thermal energy are used to split water into oxygen and hydrogen (Abifarain et al., 2024b). In this process, hydrogen is generated near the cathode and oxygen at the anode, as described by Eq. (2) (Ahmadi et al., 2022):



Table 2
PEM electrochemical equations (Husaini et al., 2025).

Term	Equation
Nernst equation	$V_0 = 1.229 - 0.00085(T_{PEM} - 298)$
Anode overpotential equation	$V_{act.an} = \frac{RT}{F} \sinh^{-1} \frac{J}{2J_{0.an}} = J_{an}^{ref} \exp\left(\frac{-E_{act.an}}{RT}\right) E_{act.an}$
Cathode overpotential equation	$V_{act.ca} = \frac{RT}{F} \sinh^{-1} \frac{J}{2J_{0.ca}} = J_{ca}^{ref} \exp\left(\frac{-E_{act.ca}}{RT}\right) E_{act.ca}$
Ohmic overpotential equation	$V_{ohm} = J \times R_{PEM} P_{PEM} = \int_0^D \frac{dx}{\sigma_{PEM}[\lambda(x)]} \lambda(x) = \frac{\lambda_{ca} - \lambda_{an}}{D} x + \lambda_{ca} \sigma_{PEM}[\lambda(x)] = [0.5139\lambda(x) - 0.326] \exp\left[1268\left(\frac{1}{303} - \frac{1}{T_{PEM}}\right)\right]$

Water electrolysis can be separated into two distinct types based on the operation's temperature: high-temperature and low-temperature electrolyzers. Proton Exchange Membrane Electrolyzers (PEME) and Alkaline Electrolyzer Cells (AEC) are the most advanced low-temperature options, with PEME offering higher efficiency, faster response times, and better performance under fluctuating power conditions, making it the preferred choice for this study. The efficiency of the PEM electrolyzer plays a critical role in minimizing the amount of electrical power needed to supply enough hydrogen for methanation. Solid oxide electrolyzers, an emerging high-temperature technology, operate effectively but remain non-commercialized. The modeling of PEME is discussed below.

The hydrogen production flow rate can be determined by the following equation (Ahhabi Saray et al., 2024):

$$\dot{n}_{H_2,out} = J/2F \quad (3)$$

In this context, J denotes the current density.

As stated in Eq. (2), the flow rate of oxygen is half of the produced hydrogen. The flow rates of water and oxygen exiting the electrolyzer is determined using the following equations:

$$\dot{n}_{O_2,out} = J/4F \quad (4)$$

$$\dot{n}_{H_2O,out} = \dot{n}_{H_2O,in} - J/2F \quad (5)$$

The electrical energy needed for the process is calculated from Eq. (6) (Balali et al., 2023):

$$E_{electric} = J \times V \quad (6)$$

$E_{electric}$ represents the input energy, while V denotes the cell potential, definable by the following equation (Husaini et al., 2025):

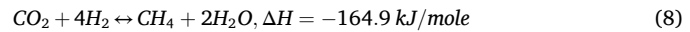
$$V = V_0 + V_{act.ca} + V_{act.an} + V_{ohm} \quad (7)$$

In this equation, V_0 represents the reversible potential determined using the Nernst equation. $V_{act.an}$, $V_{act.ca}$ and V_{ohm} correspond to the activation overpotential of the anode, activation overpotential of the cathode, and ohmic overpotential, respectively. The overpotential and Nernst equations are summarized in Table 2.

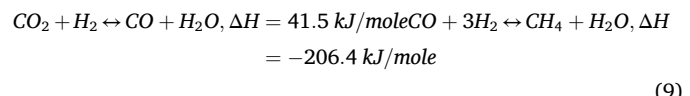
2.6. Methanation process

Methanation is the production of methane by reacting CO_2 and H_2 through the Sabatier process, typically driven by a catalyst. Recent advancements in membrane-based methanation have improved methane production efficiency through innovative reactor designs integrating selective membranes. Catalytic membrane reactors use zeolite or polyimide membranes for in-situ water removal, enhancing CO_2 conversion for purified CO_2 - H_2 feeds. Counter-current configurations have reduced membrane area requirements, lowering costs. Innovations in biological methanation include trickle-bed reactors with integrated membranes, enabling efficient biogas upgrading to more than 98 % biomethane purity, though membrane stability under continuous operation poses challenges (Yörüküü et al., 2025). The proposed system leverages catalytic membranes with purified inputs from the S-Graz cycle, avoiding biogas impurities to ensure catalyst longevity and support

carbon-circular multigeneration. In the literature, two principal processes for this process are outlined. The first mechanism involves the direct hydrogenation of CO_2 to produce methane, and the reaction occurs as follows (Toro and Sciubba, 2018):



In contrast, a more commonly observed mechanism occurs in two steps. First, carbon monoxide (CO) is formed by the water-gas shift reaction. Subsequently, CO undergoes hydrogenation to form methane. The reaction sequence is described in Eq. (9):



The methanation reaction is an exothermic process that typically occurs within a temperature range of 200–550 °C, where temperature plays a more critical role in conversion efficiency than pressure, reducing conversion and improving kinetics as it increases. This study focuses on methanation within an integrated membrane reactor using a Ru-based catalyst, which combines catalytic activity with a vapor perm-selective membrane to separate steam and syngas in situ. Compared to conventional systems, this configuration enhances CO_2 conversion by approximately 18 % under similar conditions (Jalili et al., 2023) (Ohyama et al., 1997). Precisely controlling temperature around 300 °C optimizes the performance of the reactor, leveraging its high activity for efficient methanation. Methane production is calculated using a temperature-dependent equation based on experiment and the incoming flow rate of CO_2 (Romano et al., 2014):

$$CR_{SM}(\%) = 39.25 + [0.333 \times (T_{sab} - 273.15) + (-0.0005 \times (T_{sab} - 273.15)^2)] \quad (10)$$

where, CR_{SM} is the conversion rate of CO_2 . The methane production rate can be found from Eq. (11):

$$\dot{n}_{CH4,out} = CR_{SM} \times \dot{n}_{CO2,in} \quad (11)$$

Finally, taking stoichiometric reaction into account, the mole proportions of the gases at the reactor outlet can be calculated in the following manner:

$$\dot{n}_{g,out} = (\dot{n}_{CO2,in} + \dot{n}_{H2,in}) - 2 \times \dot{n}_{CH4,out} \quad (12)$$

$$x_{CO2,out} = \frac{\dot{n}_{CO2,in} - \dot{n}_{CH4,out}}{\dot{n}_{g,out}} \quad (13)$$

$$x_{H2,out} = \frac{\dot{n}_{H2,in} - 4 \times \dot{n}_{CH4,out}}{\dot{n}_{g,out}} \quad (14)$$

$$x_{CH4,out} = \frac{\dot{n}_{CH4,in} + \dot{n}_{CH4,out}}{\dot{n}_{g,out}} \quad (15)$$

2.7. Heliostat field

The solar radiation received by a heliostat is represented by Equation

(16). Furthermore, as outlined in Eq. (17), the heliostat field directs a portion of the reflected solar energy towards the receiver, with the specific fraction of heat being determined by the reflective properties of the system (Tehrani and Taylor, 2016):

$$\dot{Q}_{HEL} = DNI \times A_{Mirror} \times N \quad (16)$$

$$\dot{Q}_{REC} = \dot{Q}_{HEL} \times \eta_{OPT} \quad (17)$$

Some of the receiver's energy is lost through various mechanisms such as convection, conduction, reflection and radiation. The receiver's energy balance is described as follows (Tehrani and Taylor, 2016):

$$\dot{Q}_{Abs} = \dot{Q}_{REC} - \dot{Q}_{loss} \quad (18)$$

$$\dot{Q}_{loss} = \dot{Q}_{Cond} + \dot{Q}_{Conv} + \dot{Q}_{Rad} + \dot{Q}_{Ref} \quad (19)$$

In order to calculate the receiver's aperture and surface area, concentration ratio (C) and view factor (Fr) are utilized. Additionally, it is important to note that the height of the receiver aperture (h) is twice the aperture thickness (w) (Saleh Kandezi and Mousavi Naeenian, 2022).

$$Fr = \frac{A_{REC,ap}}{A_{REC,sur}} \quad (20)$$

$$A_{REC,ap} = h \times w = \frac{h^2}{2} \quad (21)$$

$$C = \frac{A_{Field}}{A_{REC,ap}} = A_{HEL} \times \frac{N}{A_{REC,ap}} \quad (22)$$

The radiation heat loss from the receiver's surface can be calculated by Eq. (23) (Alirahmi et al., 2021):

$$\dot{Q}_{Rad} = \left(\frac{\epsilon_w \times \sigma \times A_{REC,sur} \times (T_{REC,sur}^4 - T_{Amb}^4)}{\left(\frac{\epsilon_w}{Fr} \right) + 1 - \epsilon_w} \right) \quad (23)$$

where σ is the constant of Stefan-Boltzmann ($5.67 \times 10^{-8} \left[\frac{W}{m^2 K^4} \right]$), and ϵ_w is the absorption coefficient of the receiver surface. Another source of cavity receiver's heat loss is the reflection of rays that leak through the aperture, which is given by Eq. (24) (Abbasi et al., 2019):

$$\dot{Q}_{Ref} = \alpha \times \dot{Q}_{REC,in} \times Fr \quad (24)$$

where α is the reflectivity factor of the receiver. Convection heat loss in cavity receivers takes place under both natural and forced flow conditions. To quantify this energy loss, it is important to apply the following mathematical formulations (Abbasi et al., 2019):

$$\dot{Q}_{Conv} = \dot{Q}_{Conv,N} + \dot{Q}_{Conv,F} \quad (25)$$

$$\dot{Q}_{Conv,N} = 0.81 \times A_{REC,sur} \times (T_{REC,sur} - T_{Amb})^{1.426} \quad (26)$$

$$\dot{Q}_{Conv,F} = h_{Conv,F} \times A_{REC,Ap} \times (T_{REC,sur} - T_{Amb}) \quad (27)$$

$$Nu_{Conv,F} = \frac{h_{Conv,F} \times H}{K_{Air}} = 0.0287 \times Re_{Conv,F}^{0.8} \times Pr_{Conv,F}^{0.333} \quad (28)$$

$$Re_{Conv,F} = \frac{\rho_{Air} \times V_{Wind} \times H}{\mu_{Air}} \quad (29)$$

$$Pr_{Air} = \frac{\mu_{Air} \times C_{P,Air}}{K_{Air}} \quad (30)$$

Among all forms of heat loss in cavity receivers, conduction results in the least energy dissipation. However, it remains significant enough to be factored into thermal calculations. A set of equations is established to quantify this loss accordingly (Abbasi et al., 2019):

$$\dot{Q}_{cond} = \frac{K_{Ins} \times A_{REC,sur}}{\delta_{Ins}} (T_{REC,sur} - T_{Ins}) = h_{Mix} \times A_{REC,sur} \times (T_{Ins} - T_{Amb}) \quad (31)$$

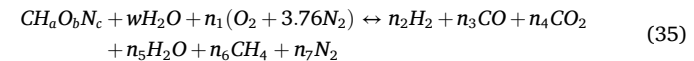
$$h_{Mix} = h_{Air,fc} + h_{Air,nc} \quad (32)$$

$$h_{Air,nc} = 1.24 \times (T_{Ins} - T_{Amb})^{0.333} \quad (33)$$

$$Nu_{Air,fc} = \frac{h_{Air,fc} \times H}{K_{Air}} = 0.02657 \times Re_{Air,fc}^{0.805} \times Pr_{Air}^{0.45} \times \left(\frac{T_{Ins}}{T_{Amb}} \right)^{0.2} \quad (34)$$

2.8. Gasifier

The process of biomass gasification involves transforming biomass into syngas, with a gasifying agent such as air or steam. The gasification reaction with air is described in Eq. (35) (Fu et al., 2024) (Zainal et al., 2001):



The biomass is expressed using its chemical composition $CH_aO_bN_c$. Additionally, w signifies the water content present in the biomass per kilomole of fuel. The type of biomass used in this study is paddy husk.

The moisture content (MC) is the ratio of the water mass to the total mass of biomass, which can be calculated by Eq. (36) (Karimi et al., 2020):

$$W = \frac{M_{biomass}MC}{18(1 - MC)} \quad (36)$$

where $M_{biomass}$ is the biomass' molar mass, and w is the water content in a kmole of biomass.

The equilibrium constants of methane formation reaction and water-gas shift reactions can be calculated based on specific thermodynamic relationships. The corresponding equations are expressed as follows:

$$K_1 = \frac{n_6}{n_2^2} \left(\frac{P/P_{ref}}{n_{tot}} \right)^{-1} \quad (37)$$

$$K_2 = \frac{n_2 n_4}{n_3 n_5} \left(\frac{P/P_{ref}}{n_{tot}} \right)^0 \quad (38)$$

K_1 and K_2 correspond to the equilibrium constants calculated from the following relationships:

$$\ln K_1 = \frac{-\Delta G_1^0}{RT_g} \quad (39)$$

$$\ln K_2 = \frac{-\Delta G_2^0}{RT_g} \quad (40)$$

ΔG_1^0 and ΔG_2^0 represent the changes in Gibbs free energy associated with the formation of methane and water-gas shift reactions, respectively, while T_g denotes the temperature of gasification.

Under the assumption that the gasification process occurs adiabatically, the energy balance can be expressed by Eq. (41) (Mojaver et al., 2023):

$$\begin{aligned} \bar{h}_{f,biomass}^0 + w \times \bar{h}_{f,H_2O}^0 + n_1(\bar{h}_{f,air}^0 + \Delta \bar{h}_{air}) &= n_2(\bar{h}_{f,H_2}^0 + \Delta \bar{h}_{H_2}) \\ &+ n_3(\bar{h}_{f,CO}^0 + \Delta \bar{h}_{CO}) + n_4(\bar{h}_{f,CO_2}^0 + \Delta \bar{h}_{CO_2}) + n_5(\bar{h}_{f,H_2O}^0 + \Delta \bar{h}_{H_2O}) \\ &+ n_6(\bar{h}_{f,CH_4}^0 + \Delta \bar{h}_{CH_4}) + n_7(\bar{h}_{f,N_2}^0 + \Delta \bar{h}_{N_2}) \end{aligned} \quad (41)$$

By utilizing the previously mentioned equations, the unknown variables from n_1 to n_7 can be resolved, allowing for the determination of the syngas composition. Once formed, the syngas enters the combustion chamber to be processed further. Under the assumption of complete

Table 3

Purchasing cost of the components of the system (Khodaei et al., 2023) (Mehrenjani et al., 2024) (Su, 2025).

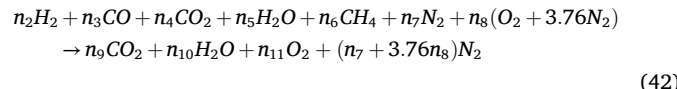
Component	Cost function
Gasifier (\$)	$1600(\dot{m}_{Biomass,hourly})^{0.67}$
Combustion chamber (\$)	$46.08 \left(\frac{\dot{m}_{Biomass}}{0.995 - \left(\frac{P_{out}}{P_{in}} \right)} \right) \times (1 + \exp(0.018 \times T_{cc} - 26.4))$
Turbine (\$)	$4750(\dot{W}_T)^{0.75}$
Heat exchangers (\$)	$309.14(A_{HE})^{0.85}$
Pumps (\$)	$200(\dot{W}_{pump})^{0.65}$
Compressors (\$)	$71.1 \left(\frac{\dot{m}_{compressor} \times r_p}{0.01} \right) \times \ln(r_p)$
Heliostat (\$)	$180 \times N_{mirrors} \times A_{mirrors}$
Receiver (\$)	$A_{rec,ap} \times (79 \times T_{Heliost.out} - 42000)$
Methanation reactor (\$)	$2.86 \times 10^6 \times \left(\frac{V_{reactor}}{0.71} \right)^{0.6}$
PEM electrolyzer (\$)	$1000 \times \dot{W}_{PEM}$
Calciner (\$)	$13140 \times Q_{Calciner}^{0.67}$
Carbonator (\$)	$16590 \times (0.15 \times Q_{Calciner})^{0.67}$
Thermal energy storage (\$/kWh)	30
CO ₂ Storage (\$/m ³)	100

Table 4

Different fuels' CO₂ emission factors (Hai et al., 2023).

Fuel type	CO ₂ emission factor (kg CO ₂ /kWh)
Propane	0.215
Butane	0.222
Butane/propane	0.218
Kerosene	0.247
Coal	0.325
Natural gas	0.181
Gasoline	0.243
Residential heating fuel	0.269

combustion, the resulting reaction is described as Eq. (42) (Mojaver et al., 2023):



In this study, nitrogen present in the flue gas is removed using filtration systems, enabling the S-Graz cycle to operate solely with CO₂ and water as working fluids.

3. Overall system performance

3.1. Energy analysis

Energy and mass balance principles are essential tools in the evaluation and optimization of multigeneration systems, ensuring that all energy and material flows are accounted for in accordance with the conservation laws. The detailed formulation of these balances for different system components is presented as follows (Mehrenjani et al., 2024) (Ghorbani et al., 2025):

$$\sum_i \dot{m}_i - \sum_e \dot{m}_e = \frac{dm_{CV}}{dt} \quad (43)$$

$$\dot{Q} - \dot{W} + \sum_i \dot{m}_i \left(h_i + \frac{V_i^2}{2} + gz_i \right) - \sum_e \dot{m}_e \left(h_e + \frac{V_e^2}{2} + gz_e \right) = \frac{dE_{CV}}{dt} \quad (44)$$

In these formulations, h represents the flow enthalpy, which is a measure of the total energy contained within a fluid stream.

Table 5

Validation of the methanation unit.

Component	Present study (mole/s)	Eisavi et al. (Eisavi et al., 2022) (mole/s)
CO _{2,out}	0.016593	0.0166
H _{2,out}	0.06637	0.06639
CH _{4,out}	0.2668	0.2668
H ₂ O _{out}	0.5336	0.5337

Table 6

Validation of the gasifier.

Component (on a dry-mole basis)	Present study (%)	Eisavi et al. (Eisavi et al., 2022)(%)	Experimental data (%)
H ₂	21.055	21.06	15.23
CO	20.4361	19.61	23.04
CH ₄	1.127	0.997	1.58
CO ₂	10.2844	12.43	16.42
N ₂	36.86	44.56	42.03
RMSE (%)	4.582	3.699	—

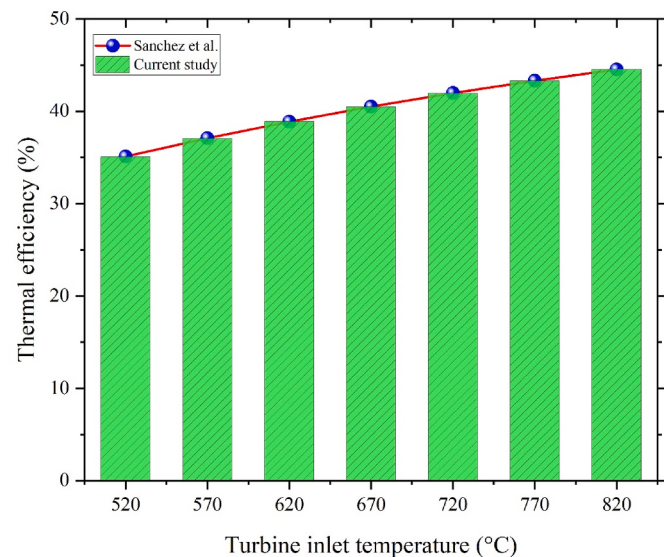


Fig. 3. Validation of the Supercritical CO₂ cycle with the work of Sanchez et al. (Sánchez et al., 2012).

3.2. Exergy analysis

Exergy analysis is a comprehensive thermodynamic approach used to evaluate the sustainability and efficiency of energy systems by accounting for the capacity and quality of energy to perform useful work. To systematically analyze exergy within a system, an balance of exergy is formulated, expressed as Eq. (45) (Zhang et al., 2025b):

$$\dot{E}_Q + \sum_i \dot{m}_i ex_i = \sum_e \dot{m}_e ex_e + \dot{E}_W + \dot{E}_D \quad (45)$$

The exergy of a flow stream comprises physical exergy and chemical exergy, representing the available energy due to pressure and temperature differences, as well as the chemical potential of the substances involved:

$$ex_i = ex_{phi} + ex_{chi} \quad (46)$$

For gas mixtures, chemical exergy is calculated by considering the contribution of each component based on its concentration and standard chemical exergy:

Table 7
Validation of the TCES.

Parameter	Present study	Ortiz et al. (Ortiz et al., 2021)	Error (%)
\dot{m}_{CO_2} (kg/s)	32.4359	32.45	0.04
\dot{m}_{CaCO_3} (kg/s)	275.2137	275.67	0.16
\dot{m}_{CaO} (kg/s)	307.6496	308.12	0.15

Table 8
Validation of the heliostat field.

Parameter	Current study	Kandezi et al. (Saleh Kandezi and Mousavi Naeenian, 2022)	Error (%)
Area of the heliostat field(m ²)	306234	296468	3.3
Area of the receiver surface (m ²)	402.124	412	2.4
Area of the receiver aperture (m ²)	345.57	330	4.72
Receiver efficiency (%)	85	89	4.5

$$ex_{ch,gas\ mixture} = \sum x_i ex_{ch,i}^0 + RT_0 \sum x_i \ln(x_i) \quad (47)$$

To calculate the system's exergy efficiency, Eq. (48) is considered:

$$\eta_{Exergy} = \frac{\dot{Ex}_{Products}}{\dot{Ex}_{Supplied}} = 1 - \frac{\dot{Ex}_{Destroyed}}{\dot{Ex}_{Supplied}} \quad (48)$$

The total exergy destroyed by the components of the system is expressed in Eq. (49):

$$\begin{aligned} \dot{Ex}_{Destroyed} = & \dot{Ex}_{Destroyed,Gasifier} + \dot{Ex}_{Destroyed,S-Graz} + \dot{Ex}_{Destroyed,Heliostat} \\ & + \dot{Ex}_{Destroyed,Receiver} + \dot{Ex}_{Destroyed,TCES} + \dot{Ex}_{Destroyed,CCU} + \dot{Ex}_{Destroyed,S-CO_2} \\ & + \dot{Ex}_{Destroyed,PEM} + \dot{Ex}_{Destroyed,Methanator} \end{aligned} \quad (49)$$

3.3. Economic analysis

In economic evaluation, assessing the overall cost rate of a system requires defining cost functions for each individual component. By incorporating these costs, the overall cost rate, typically measured in dollars per hour, is determined by Eq. (50) (Mehrenjani et al., 2022):

$$\dot{Z}_{tot} = \frac{CRF \times \varphi \times \sum_k Z_k}{t_{hour}} \quad (50)$$

Within this formula, Z_k signifies the acquisition expense of component k, outlined in Table 3, while t_{hour} indicates the system's yearly operating duration. The factor φ , assigned a value of 1.06, accounts for maintenance considerations. Moreover, CRF represents the capital recovery factor, an essential variable calculated by Eq. (51) (Mehrenjani et al., 2022):

$$CRF = \frac{i(1+i)^n}{(1+i)^n - 1} \quad (51)$$

In this context, the symbol i stands for the rate of interest. The term n signifies the service life of the components of the system, directly impacting cost estimations. The following equations fulfill a distinct role by adjusting initial equipment expenses to their present value, integrating the cost index of equipment to reflect cost variations over time (Jabraelzadeh et al., 2025):

$$cost\ at\ present\ year = original\ cost \times \frac{cost\ index\ of\ the\ present\ year}{cost\ index\ of\ the\ base\ year} \quad (52)$$

Table 9
Validation of the S-Graz cycle.

	Current study	Nami et al. (Nami et al., 2019)	Error (%)
HTT power (kW)	3681.4	3879	5.1
HPT power (kW)	277.32	278.9	0.57
LPT power (kW)	483.4	498.3	3
Compressor power consumption (kW)	1487.4	1466.5	1.4
Pump power consumption (kW)	17.418	17.44	0.13

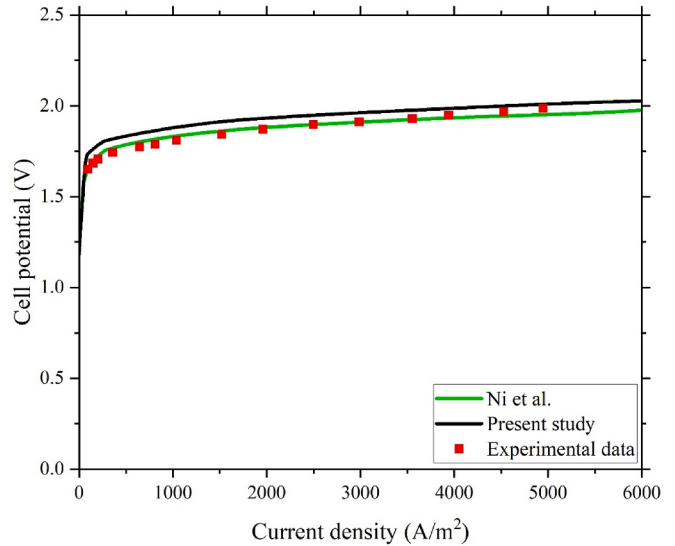


Fig. 4. Validation of the PEM electrolyzer with the work of Ni et al. (Ni et al., 2008).

$$Z_{2025} = Z \frac{CI_{2025}}{CI_{reference}} \quad (53)$$

here, $CI_{reference}$ denotes the current year's cost index.

Some important economic factors for the system are capital investment cost, Net Present Value (NPV), Internal Rate of Return (IRR), Simple Payback Period (SPP), and Levelized Cost Of Electricity ($LCOE$), which are calculated by the following equations (Ehyaei et al., 2021):

$$NPV = \frac{\text{Annual Income} \times (1 - (1+r)^{-n})}{r} - \text{Initial Investment} \quad (54)$$

$$IRR = \frac{\text{Annual Income}}{\text{Initial Investment}} \left(1 - \frac{1}{(1+IRR)^n} \right) \quad (55)$$

$$SPP = \frac{\text{Initial Investment}}{\text{Annual Income}} \quad (56)$$

$$LCOE = \frac{AOC_{power}}{\dot{W}_{net,power}} \quad (57)$$

In these formulations, r , n , AOC_{power} and $\dot{W}_{net,power}$ represent the discount rate (6 %), lifetime (30 years), annual operation cost of the power generation subsystems and net power generation of the power generation subsystems, respectively.

3.4. Environmental analysis

The polygeneration system considered in this research utilizes biomass and solar energy as its energy sources. No traditional fossil fuel is used, so the system saves the emission of CO_2 . CO_2 emission factors of

Table 10

Essential values for the simulation of the systems and major outputs of the simulation (Nami et al., 2019) (Tehrani and Taylor, 2016) (Zainal et al., 2001) (Ortiz et al., 2019).

Simulation input values		
Section	Parameter	Value
Ambient	Ambient temperature (K)	298.15
	Ambient pressure (kPa)	101.3
Gasifier	Gasification temperature (K)	700
	Gasification pressure (bar)	60.8
S-Graz	Moisture content (%)	20
	Flow rate of biomass (kg/h)	2000
S-Graz	Combustion chamber outlet temperature (K)	1673
	Turbine efficiencies (%)	90
	Compressor efficiencies (%)	90
	Pump efficiencies (%)	72
	HTT inlet pressure (bar)	40
	HTT outlet pressure (bar)	1
	LPT outlet pressure (bar)	0.04
	Sabatier temperature (K)	573
	PEM membrane thickness (m)	5×10^{-5}
	Anode activation energy (J/mole)	76000
PEM electrolyzer	Cathode activation energy (J/mole)	18000
	DNI (W/m ²)	766
Heliostat field	Number of mirrors	300
	Mirror surface area (m ²)	121
	Heliostat cycle upper pressure (bar)	240
	Heliostat cycle lower temperature (bar)	60
	Heliostat inlet temperature (K)	900
	Recuperator effectiveness	0.95
	S-CO ₂ compressor inlet pressure (bar)	75
	S-CO ₂ compressor outlet pressure (bar)	25
	Solar heat saved percentage in TCES (%)	50
	Main outputs of the simulation	
Parameter	Value	
	Daytime	Nighttime
S-Graz net power (MW)	2.78	2.78
S-Graz total heat dissipation (MW)	2.28	2.28
Methane production (kg/h)	966.55	966.55
Heliostat field total heat dissipation (MW)	5.97	4.02
Saved heat by TCES (MW)	6.31	–
Heat dissipated by TCES (MW)	–	6.31
CO ₂ flow rate towards carbon capture unit (kg/s)	1.78	–
CO ₂ flow rate towards TCES (kg/s)	–	1.78
Carbon capture unit power consumption (MW)	0.83	–
Carbon capture unit power generation (MW)	–	0.166
S-CO ₂ cycle power generation (MW)	2.44	0.98
S-CO ₂ cycle heat dissipation (MW)	3.86	1.55
Net power generation (MW)	2.37	1.90
Exergy efficiency (%)	33.99	49.87
Total heating generation (MW)	11.97	7.71
Exergy destruction (MW)	32.7	18.59
Total cost rate (\$/h)	757.92	385.97
Saved emissions rate (kg CO ₂ /h)	429.27	345.13

various fossil fuels are mentioned in Table 4. The CO₂ emission rate of saving for the proposed system is calculated in the following manner:

$$\Delta\dot{m}_{CO_2} = \dot{W}_{net} \times e_{CO_2} \quad (58)$$

Here, e_{CO_2} denotes the CO₂ emission factor.

In this study, the baseline fossil fuel is chosen to be natural gas, due to its widespread availability and common use in conventional power plants.

4. Validation

To validate the accuracy of the simulation results across different system components, the simulation findings from this research were compared with relevant research. Table 5 shows the comparison results of this study's findings to that of Eisavi et al. (2022) regarding the performance of the methanation unit. The table highlights the accuracy

Table 11

Thermophysical properties of each state of the proposed systems.

State	Fluid	Temperature (K)	Pressure (kPa)
1	Biomass	298.1	101.3
2	Air	298.1	101.3
3	Syngas	700	6080
G1	CO ₂ , H ₂ O	1673	4000
G2	CO ₂ , H ₂ O	1034.7	100
G3	CO ₂ , H ₂ O	790	100
G4	CO ₂ , H ₂ O	475	4
G5	H ₂ O	302.1	100
G6	H ₂ O	302.1	100
G7	H ₂ O	302.1	100
G8	H ₂ O	302.1	100
G9	H ₂ O	304.2	18000
G10	H ₂ O	650	18000
G11	H ₂ O	523.7	4000
G12	CO ₂ , H ₂ O	790	100
G13	CO ₂ , H ₂ O	1601.4	4000
G14	CO ₂	302.1	4
G15	CO ₂	792.12	202.6
G16	CO ₂	523	202.6
P1	H ₂ O	298.1	202.6
P2	O ₂	353	202.6
P3	H ₂	353	202.6
P4	H ₂	523	202.6
H1D	CO ₂	900	24000
H2D	CO ₂	1400	24000
H3D	CO ₂	1210.7	24000
H4D	CO ₂	1017.6	24000
H5D	CO ₂	832.81	6000
H6D	CO ₂	630	6000
S1	CO ₂	637.3	22500
S2	CO ₂	850	22500
S3	CO ₂	717.4	7500
S4	CO ₂	401.78	7500
S5	CO ₂	308.1	7500
S6	CO ₂	386.22	22500
C1D	CO ₂	1223.2	100
C2D	CO ₂	308.1	100
C3D	CO ₂	769.9	7500
C4D	CO ₂	298.1	7500
H1N	CO ₂	736	24000
H3N	CO ₂	1150	24000
H4N	CO ₂	900	24000
H5N	CO ₂	729.8	6000
H6N	CO ₂	550	6000
C1N	CO ₂	298.1	7500
C2N	CO ₂	375.6	7500
C3N	CO ₂	227.14	800
C4N	CO ₂	1223.2	800

of the methanator's simulation, having less than 1 % error when compared with the mentioned reference. Furthermore, in order to assess the gasifier's performance, the research of Eisavi et al. (2022) has been used as a benchmark for this study. Table 6 compares these findings. In Fig. 3, the validity of the supercritical CO₂ cycle has been checked with Sanchez et al. (Sánchez et al., 2012). Moreover, Table 7 outlines the reliability of TCES compared to Ortiz et al. (2021). Table 8 highlights the validation of the heliostat with regards to Kandezi et al. (Saleh Kandezi and Mousavi Naeenian, 2022). The accuracy of the S-Graz cycle model has been validated by comparing its results with Nami et al. (2019), as presented in Table 9. The table shows that the maximum error occurring in the simulation is 5.1 %, which highlights the reliability of the model. The validity of the PEM electrolyzer has been verified by comparing the results of this research with that of Ni et al. (2008) in Fig. 4.

5. Results and discussion

5.1. Results of the base system

The input parameters used for the system simulation and the major outputs of the simulation are summarized in Table 10. Furthermore, the

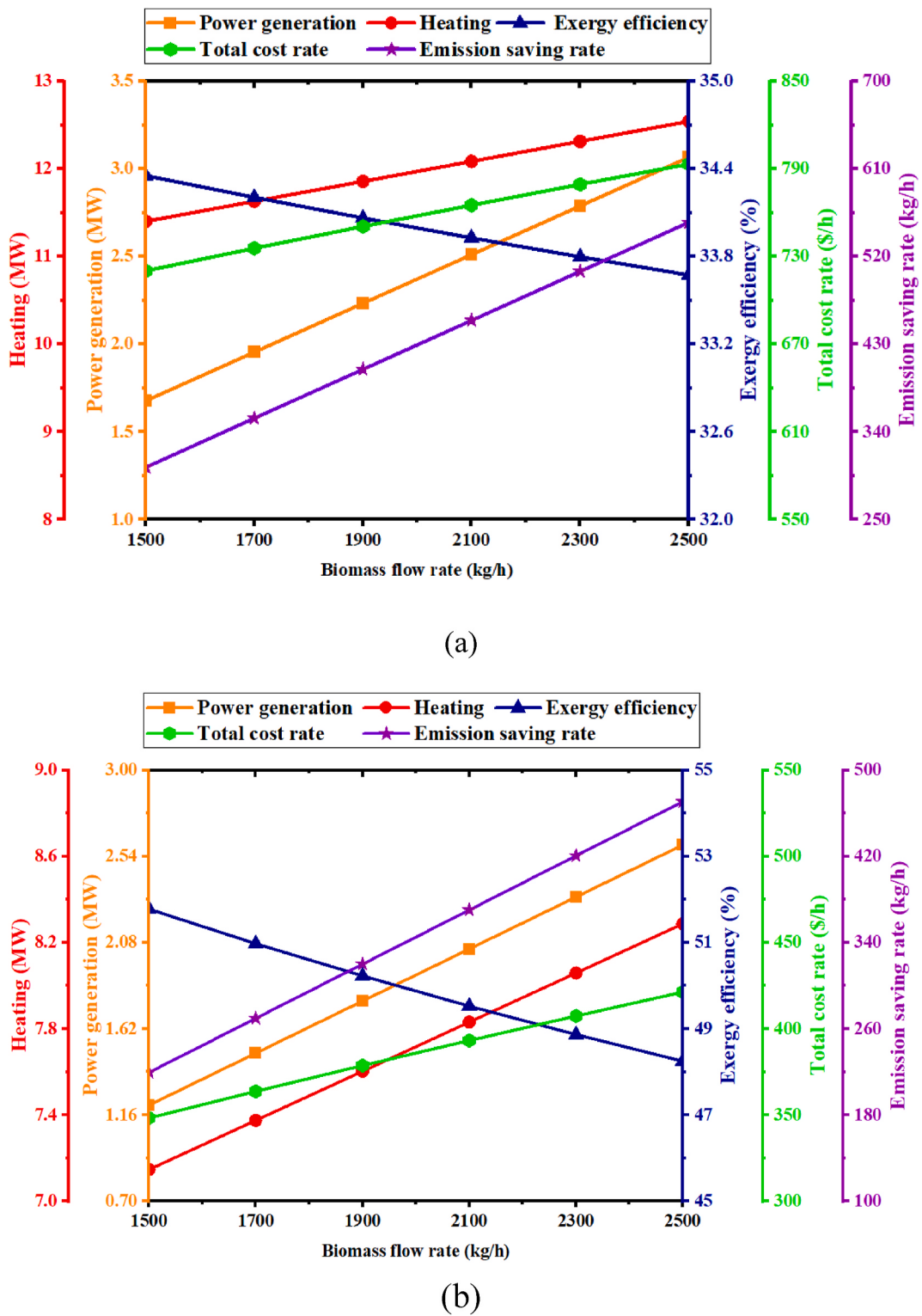


Fig. 5. The effect of the biomass feed rate on the system's performance operating during a) daytime b) nighttime.

thermochemical properties corresponding to each point within the two temporal modes are detailed in Table 11.

5.2. Parametric study

5.2.1. Effect of the biomass flow rate

Fig. 5 highlights the impact of biomass feed rate on key system outputs during both daytime and nighttime operations. As depicted in

Fig. 5(a), raising biomass feed to the gasifier from 1500 kg/h to 2500 kg/h yields a substantial improvement in net power output during the day—an approximate increase of 83 %, from 1.67 MW to 3.06 MW. This performance gain is primarily driven by the corresponding rise in the flow rate of the working fluid within the S-Graz cycle. However, this enhancement is accompanied by a 73.1 \$/h increase in operational cost, climbing from 720.2 \$/h to 793.3 \$/h, attributable to the greater energy demand of the intensified cycle.

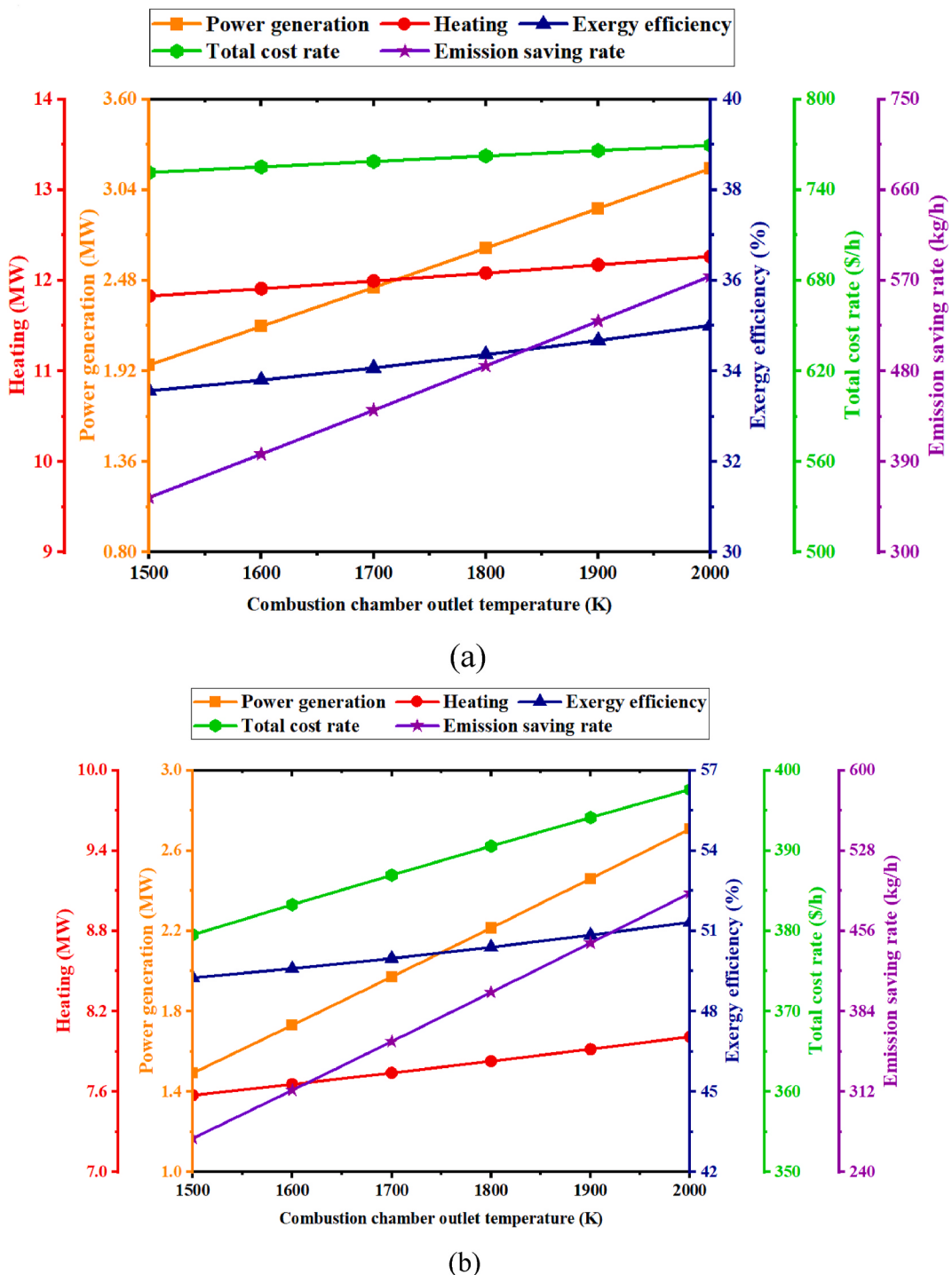


Fig. 6. The effect of the combustion chamber flue gas temperature on the system's performance operating during a) daytime b) nighttime.

As depicted in Fig. 5(b), the rise in biomass input also leads to a significant improvement in avoided CO₂ emissions. The emission savings grow by 251.4 kg CO₂/h, reaching 470.83 kg CO₂/h—an enhancement enabled by the system's increased capacity for clean electricity generation. It is also noteworthy that the variation in biomass flow exerts minimal influence on the system's total heat output, as most heat transfer occurs internally within the S-Graz cycle, particularly between the gas and steam cycle segments, with limited external dissipation.

5.2.2. Effect of the combustion chamber outlet temperature

The influence of the combustion chamber flue gas temperature on system performance is illustrated in Fig. 6. As is shown in Fig. 6(a), elevating the flue gas temperature from 1500 K to 2000 K results in a 62 % increase in daytime power generation, rising from 1.96 MW to 3.17 MW. This substantial improvement is largely attributable to the enhancement of the HTT inlet temperature, which augments the cycle's thermal efficiency. Meanwhile, the total cost rate experiences only a modest increase of 18.1 \$/h, from 751.5 \$/h to 769.6 \$/h. Nevertheless, this temperature rise is constrained by the operational limits of the system's materials.

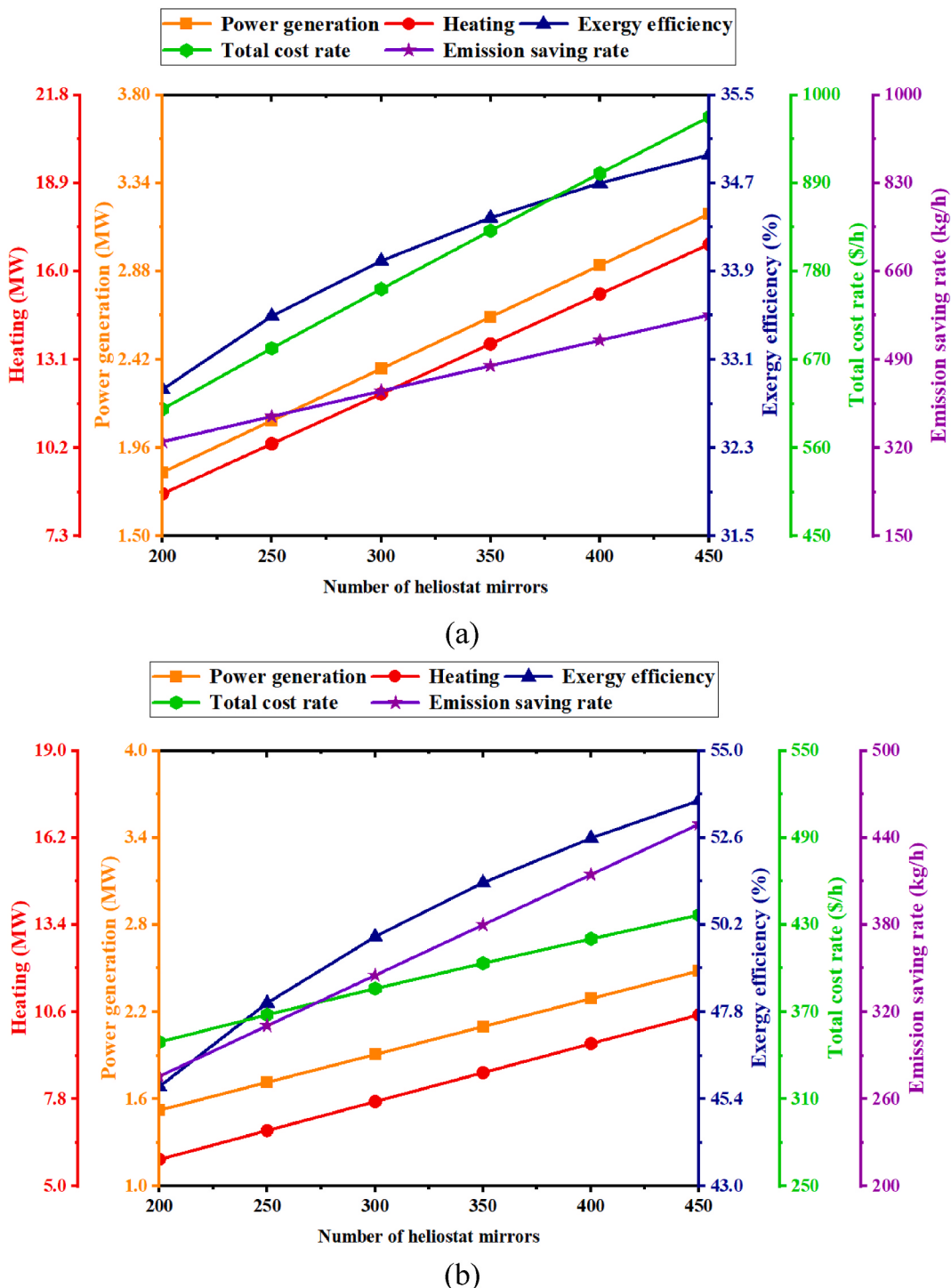


Fig. 7. The effect of mirror numbers on the system's performance operating during a) daytime b) nighttime.

During nighttime operation, as presented in Fig. 6(b), the same increase in combustion chamber temperature produces a gain of 1.21 MW in net power output, representing a roughly 81 % improvement, reaching 2.71 MW. Concurrently, the avoided CO₂ emissions increase by 219.9 kg CO₂/h, reaching a total of 490 kg CO₂/h—underscoring the benefits of higher thermal input on renewable electricity generation.

5.2.3. Effect of the number of mirrors

Fig. 7 examines the influence of heliostat mirror quantity on overall system performance. As depicted in Fig. 7(a), increasing mirror numbers from 200 to 450 enhances the thermal output by nearly 94 %,

approximately doubling it from 8.69 MW to 16.9 MW. However, this performance gain incurs a significant rise in the cost rate, which escalates by 364.5 \$/h, from 608.2 \$/h to 972.7 \$/h. This increase is primarily due to the heliostat field comprising a substantial proportion of the system's capital and operational expenses.

During nighttime, Fig. 7(b) shows that the expanded mirror field enables more solar heat to be stored during daytime operation, resulting in an electric power output increase of 0.96 MW, reaching 2.48 MW. Correspondingly, the avoided CO₂ emissions grow by 63 %, from 275.65 kg CO₂/h to 449.36 kg CO₂/h, emphasizing the effectiveness of enhanced solar collection on emission reduction.

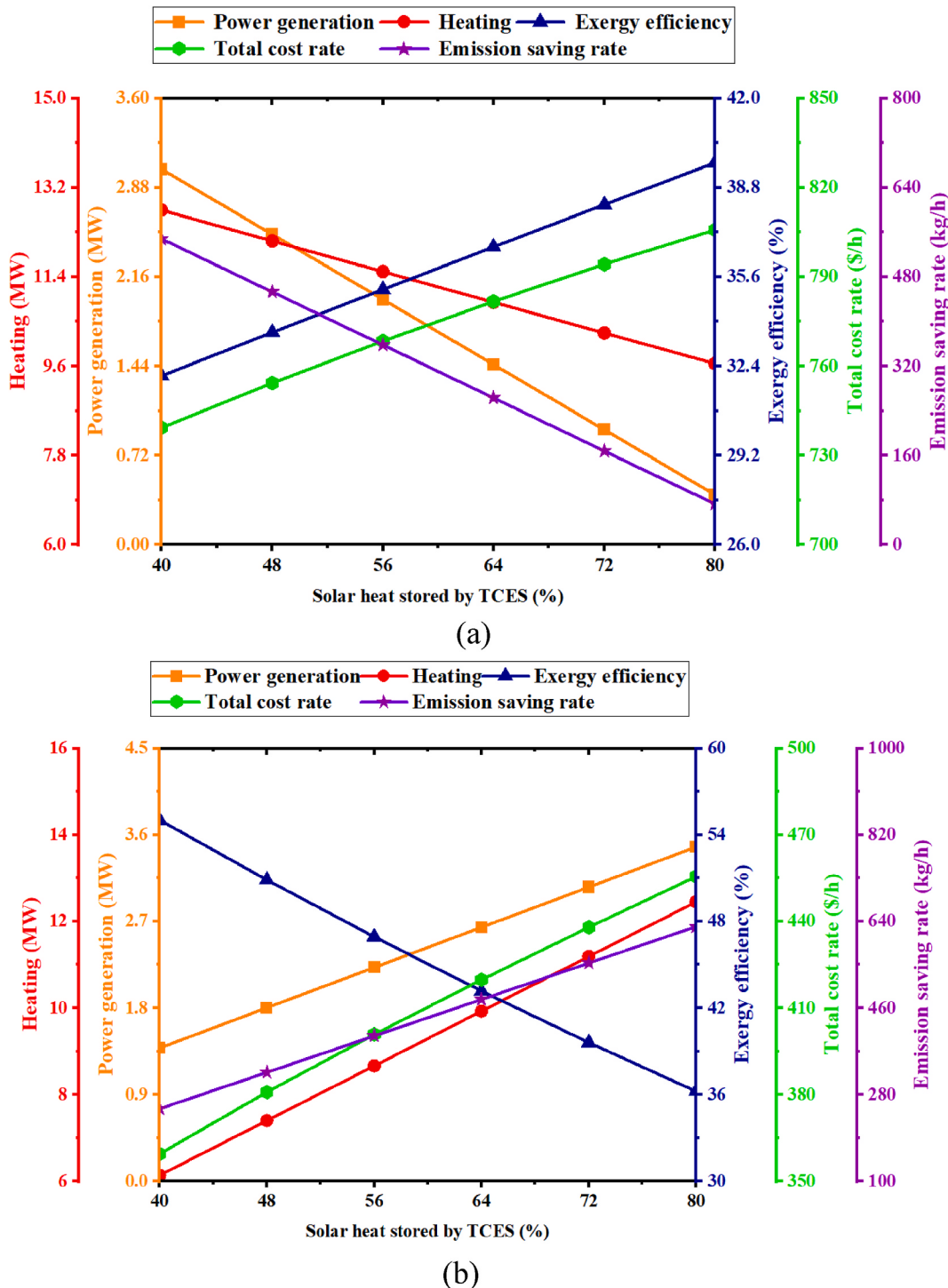


Fig. 8. The effect of the solar heat saved percentage on the system's performance operating during a) daytime b) nighttime.

5.2.4. The fraction of saved solar heat in TCES during daytime

Fig. 8 investigates how varying the proportion of solar heat stored in the TCES system affects system performance. In Fig. 8(a), increasing the storage fraction from 40 % to 80 % results in a sharp reduction of power output, falling from 3.02 MW to 0.4 MW. This reduction is also reflected in the system's thermal output due to decreased heat input into the S-CO₂ cycle. However, this change significantly enhances the exergy efficiency, which climbs by 7.64 %, from 32.05 % to 39.69 %, attributable to the lower irreversibility associated with higher-temperature heat transfer in the heliostat field.

At night, however, as shown in Fig. 8(b), increasing the percentage of stored heat leads to a decrease in exergy efficiency from 55.02 % to 36.22 %, representing a 34 % relative reduction. This decrease is directly attributed to the increased heat transfer within the integrated system. Consequently, the system experiences an enhanced power output, which rises from 1.38 MW to 3.43 MW, reflecting a significant 148 % relative improvement. This improvement occurs because the higher heat storage in the TCES results in more heat being delivered to the S-CO₂ cycle, thereby boosting its performance.

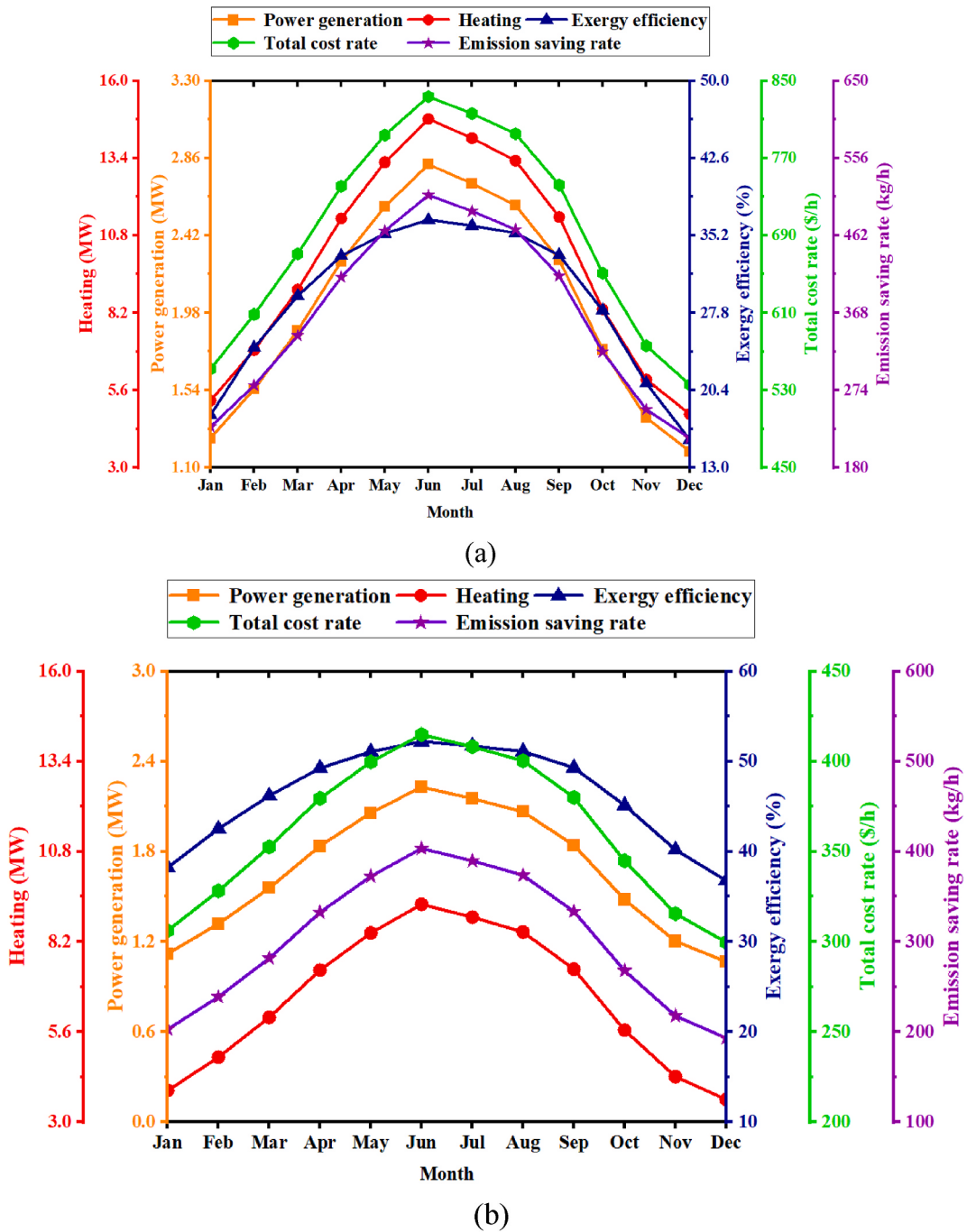


Fig. 9. Operation characteristics of the systems throughout the year operating during a) daytime b) nighttime.

5.3. Dynamic analysis of the systems' performance

Above all, it is worth mentioning that the solar irradiation data employed in this analysis were obtained from Meteonorm, a well-established software tool designed to provide time-series-based accurate climatic data for locations worldwide, across various time scales.

Fig. 9(a) presents the performance of the system during daytime operation across different months in central Tehran, Iran. As illustrated, the system achieves its highest performance in June, corresponding to the period with the greatest availability of direct normal irradiance (DNI) throughout the year. Specifically, in June, with an average DNI of 940.17 W/m² over an 8-h operational window, the system reaches a peak electricity output of 2.82 MW. Conversely, the lowest power output

occurs in December, declining to 1.19 MW, driven by significantly reduced solar availability.

Fig. 9(b) depicts the system's nighttime performance over the same monthly range. Again, the highest output is observed in June, related to the increased amount of energy stored in the TCES system during the day. Higher DNI in June enables greater energy capture and storage, which in turn supports enhanced energy conversion during nocturnal operation. Interestingly, the system exhibits higher average exergy efficiency at night compared to daytime, with the maximum exergy efficiency during nighttime operation reaching 52.21 %, compared to the daytime peak of 36.7 %.

As previously discussed, the highest levels of direct normal irradiance (DNI) are recorded in June. To further explore the system's

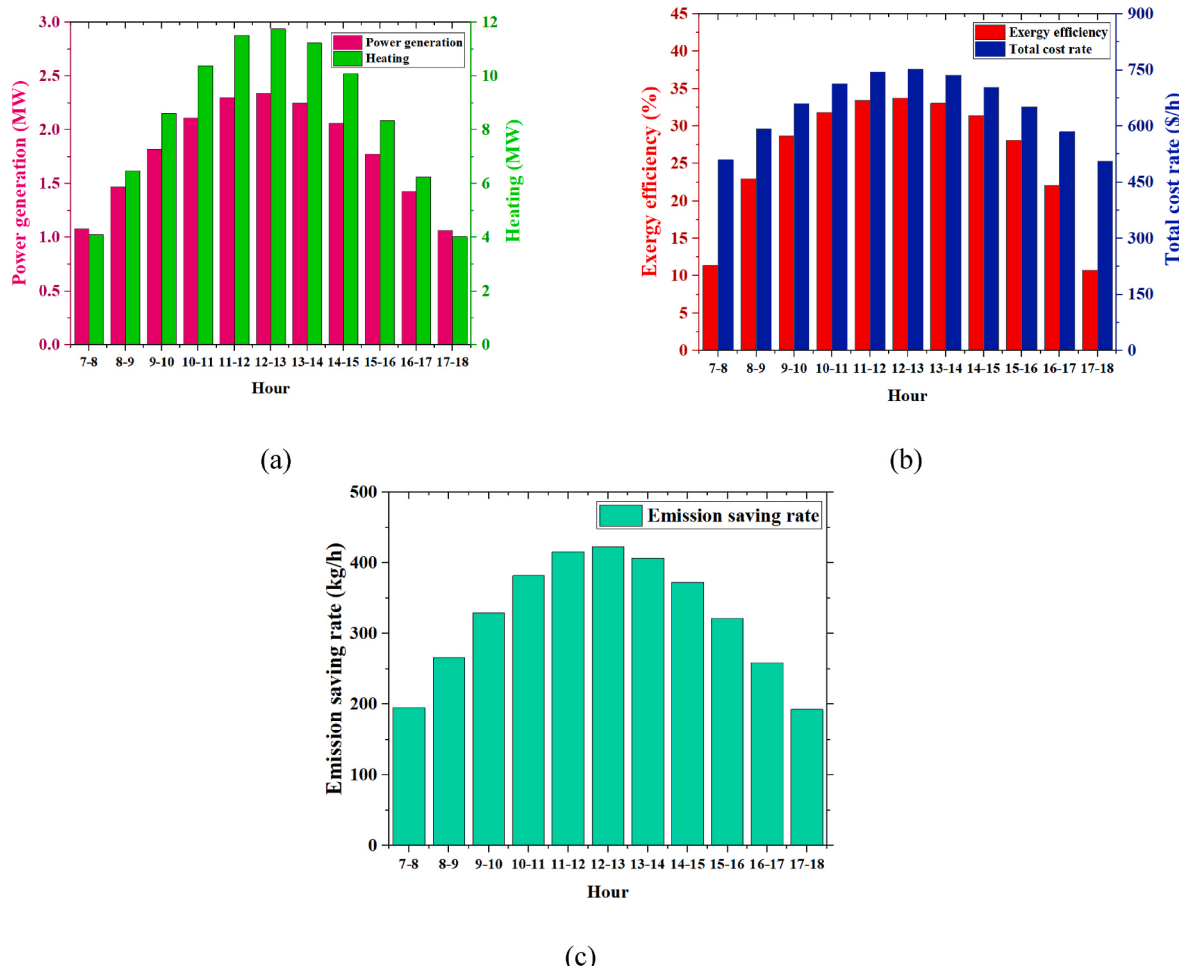


Fig. 10. Analysis of the system's a) heating and electricity output, b) exergy efficiency and total cost rate, and c) rate of emission saving throughout July 15th.

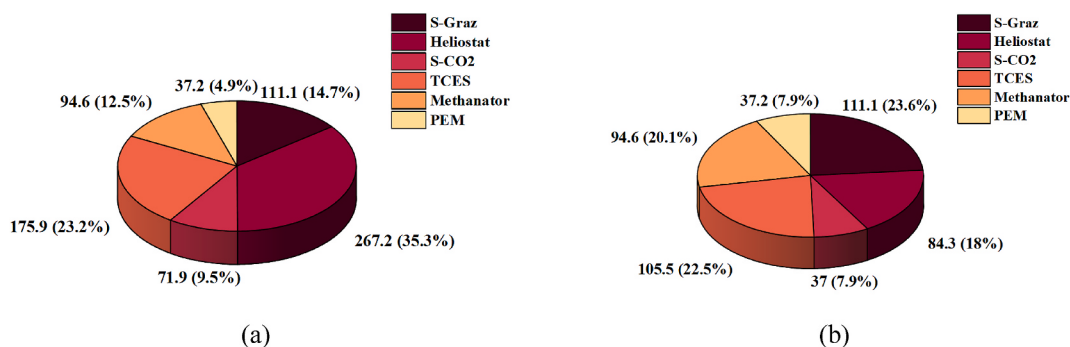


Fig. 11. The overall cost rate of different components of the systems operating at a) daytime and b) nighttime.

Table 12
Economic evaluation of the systems.

Parameter	Value
Capital Investment Cost (10^6 \$)	30.34
Net Present Value (10^5 \$)	44.83
Internal Rate of Return (%)	20.53
Simple Payback Period (years)	6.03
LCOE (cents/kWh)	8.01

performance throughout a typical day, July 15th has been selected as a representative date for detailed hourly analysis.

Fig. 10 provides an overview of the system's daytime operation on this date, focusing on key performance indicators. Fig. 10(a) presents the variation in power generation and heat dissipation throughout the day under solar irradiation. The system reaches its peak output between 12:00 and 13:00, producing 2.33 MW of electricity and 11.75 MW of heating.

Fig. 10(b) illustrates the trends in exergy efficiency and overall cost rate over the same period. Between 07:00 and 13:00, exergy efficiency rises by 22.32 %, while the overall cost rate rises by 241.7 \$/h. Both

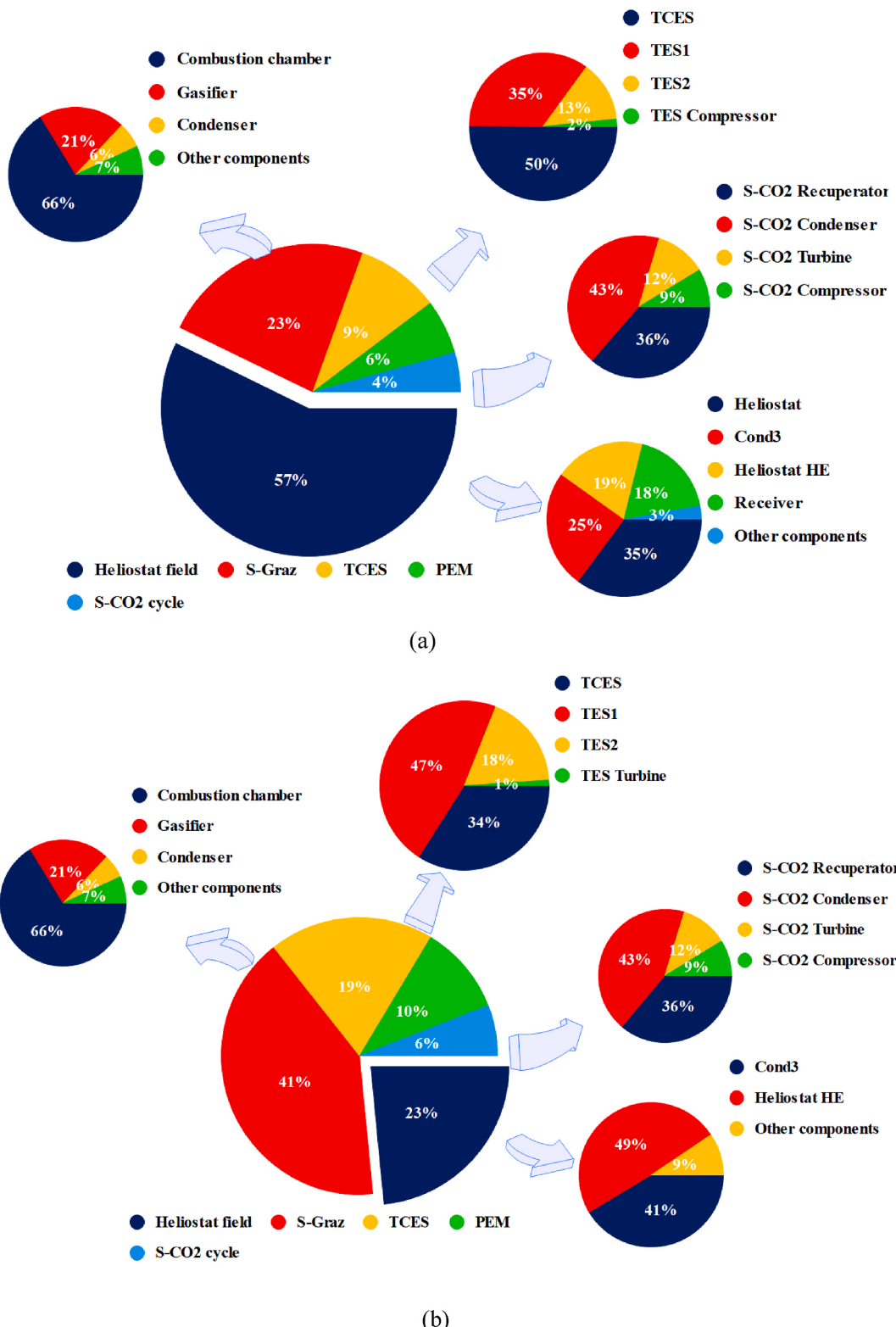


Fig. 12. Relative exergy destruction portion of different subsystems of the system working at a) daytime and b) nighttime.

metrics subsequently decline, reaching their respective minimum values by 18:00.

Fig. 10(c) shows the temporal variation in the system's emission saving rate. The highest emission reduction occurs between 12:00 and 13:00, reaching 422.9 kg CO₂ per hour. In contrast, the lowest emission saving is observed between 17:00 and 18:00, dropping to 192.76 kg CO₂ per hour—approximately 45 % of the peak value.

5.4. Economic assessment of the system

Fig. 11 illustrates how individual system components contribute to the total cost rate during both daytime and nighttime operation. As shown in Fig. 11(a), the most cost-intensive element during daytime operation is the heliostat field and its associated components, accounting for 35.3 % of the total cost rate, equivalent to 267.24 \$/h. This is

Table 13

Comparative analysis of scenarios A and B.

Parameter	Daytime operation		Nighttime operation	
	Scenario A	Scenario B	Scenario A	Scenario B
Net power generation (MW)	2.37	4.39	1.91	3.93
Total heat dissipation (MW)	11.97	11.84	7.72	7.59
Exergy efficiency (%)	33.99	35.35	49.87	52.90
Total cost rate (\$/h)	757.92	626.12	385.97	254.17
Saved emissions (kg CO ₂ /h)	429.27	795.36	345.13	711.23

followed by the TCES unit, which contributes 23.2 % of the total cost rate.

In contrast, Fig. 11(b) reveals that during nighttime operation, the largest share of the total cost rate shifts to the S-Graz cycle, representing 23.6 % of the total. This shift is primarily due to the inactivity of the heliostat field at night, as it no longer performs solar heat collection, thereby significantly reducing its contribution to the cost structure.

It is also noteworthy that the PEM electrolyzer is the least expensive component to operate in daytime mode, contributing to just 4.9 % of the total cost rate. The subsystem having the smallest share in total cost rate of the nighttime mode is the S-CO₂ cycle, with 7.9 %.

Table 12 lists the consolidated economic evaluation of the system, incorporating a weighted average of performance across 12 h of daytime and 8 h of nighttime operation, with an average total DNI of 400 W/m² during daytime operation. The capital investment cost of the integrated configuration is calculated at \$30.34 million, accounting for the combined infrastructure of solar-driven and biomass-supported subsystems, including thermal storage, methanation, and power generation units. Over a 30-year lifetime, the proposed system achieves an NPV of \$44.83 million, demonstrating strong long-term profitability and cost recovery potential. The IRR stands at 20.53 %, which exceeds typical discount rates applied in industrial investment scenarios, suggesting that the system is financially attractive under baseline assumptions.

The combined system achieves a remarkably short SPP of just 6.03 years, underscoring its rapid capital recovery despite the complexity of integrating advanced multigeneration technologies. Moreover, the LCOE stands at 8.01 cents/kWh, making this configuration highly competitive with both conventional renewables and fossil-fuel options—especially when its concurrent production of heat and green methane is taken into account. Taken together, these economic indicators demonstrate that the proposed dual-mode operation not only delivers robust financial returns but also provides a technically sound and flexible pathway for industrial-scale renewable integration and substantial emissions reduction.

5.5. Exergy assessment of the system

Fig. 12 presents the exergy destruction rates of each major system component under both daytime and nighttime operation. As shown in Fig. 12(a), during daytime operation, the heliostat cycle has the largest share of exergy destruction, with approximately 18.7 MW. In contrast, the S-CO₂ cycle contributes the least to exergy destruction, with a value of around 1.4 MW.

Fig. 12(b) highlights the changes in exergy destruction during nighttime operation. Owing to the unavailability of solar irradiation, the exergy destruction associated with the heliostat field drops substantially to approximately 4.36 MW. In this mode, the lowest exergy destruction is again observed in the recuperative S-CO₂ cycle, which dissipates about 1.11 MW of exergy.

5.6. Comparative assessment: with vs. without green methane synthesis

In this sector, the system's performance is analyzed in daytime and

nighttime operation in two different modes: A) the system uses a portion of its generated power to produce green methane, or B) no methane is to be produced by the system. Table 13 summarizes the findings of this investigation.

As Table 13 suggests, if the system operating at daytime is supposed to store CO₂ rather than convert it to green methane, about 2.02 MW of power will be saved, since there is no need for water electrolysis in this scenario. This is also the case for nighttime operation, since the S-Graz cycle operates in the same manner in nighttime as in daytime. The table also reveals that this slightly reduces the total heat dissipated by the system at both nighttime and daytime operations, while improving its exergy efficiency by 1.36 % and 3.03 % at day and night, respectively. It can be found that the overall system cost rates drop by about 130 \$/h, since there will be no need for PEM electrolyzer, methanation reactor and their related components, which leads to roughly 30 % cut in costs of the system operating at night. As with scenario B, more power can be generated renewably, the saved emission rate is also drastically improved for the systems.

It can be seen that the performance of the systems generally improves if no methane is to be produced. However, it should be noted that several advantages come with green methane production by the systems. Above all, in contrast with power and heat, methane is easily storable and dispatchable. Methane is able to act as a chemical battery, storing biomass and solar energy for use during grid peaks, which enables long-term energy security. Furthermore, methane can be fed into existing gas infrastructure, which enables decarbonization of transport, industry and buildings that can't switch to electricity with ease. Methane can be compressed, liquefied and exported, which enables the renewable system to act as a global energy player. On top of that, methanation provides a pathway for CO₂ recycling, which contributes to a circular carbon economy, especially important for net-zero frameworks.

6. Conclusion

This study presents a novel biomass-solar hybrid multigeneration system producing heating, power, and green methane while capturing and reusing CO₂ emissions. The system integrates advanced thermodynamic and renewable energy components, including the S-Graz cycle, a S-CO₂ cycle, a heliostat field, a thermochemical energy storage system on the basis of CaCO₃/CaO reaction, a PEM electrolyzer, and a methanation reactor. Two operational modes are examined: a daytime configuration reliant on solar input, and a nighttime mode powered by stored thermal energy from the TCES unit.

A thorough 4E analysis was conducted to analyze system performance under both temporal modes. Main findings are summarized below.

- At base system conditions, the daytime system reaches an electricity output of 2.37 MW, 11.97 MW of heating, and 966.55 kg/h of green methane, with a total cost rate of 757.92 \$/h.
- At nighttime, the system yields a lower power output of 1.90 MW at the same conditions, alongside methane production rates, achieving a lower overall cost rate of 385.97 \$/h owing to the absence of solar irradiation.
- Considering the base system model, exergy efficiencies for the system is 33.99 % during the day and 49.87 % at night, with corresponding CO₂ emission savings of 429.27 kg/h and 345.13 kg/h.
- Economic assessment shows an NPV of \$44.83 million and a favorable IRR of 20.53 %, while achieving an LCOE of 8.01 cents/kWh and an SPP of 6.03 years.
- Parametric and sensitivity analyses underscore the influence of factors such as biomass feed rate, combustion temperatures, heliostat field size, and heat storage percentage on energy output, cost rate, and CO₂ emission reductions.

By integrating renewable inputs and carbon recycling mechanisms,

this hybrid configuration offers a viable, low-emission pathway for multigeneration in industrial applications. The system's ability to provide multiple energy vectors—electricity, heat, and methane—simultaneously enhances its economic and operational resilience. Moreover, its modularity and adaptability to diverse climatic conditions position it as a scalable solution for decarbonized energy infrastructure.

CRediT authorship contribution statement

Arman Adouli: Writing – original draft, Validation, Software, Methodology, Investigation, Formal analysis, Data curation. **Ayat Gharehghani:** Writing – review & editing, Supervision, Resources, Project administration, Funding acquisition, Conceptualization. **Jabraeil Ahbabí Saray:** Writing – review & editing, Writing – original draft, Resources, Formal analysis. **Amirali Shirzad:** Writing – original draft, Validation, Formal analysis. **Amin Mahmoudzadeh Andwari:** Writing – review & editing, Resources, Funding acquisition.

Declaration of competing interest

The authors declare that they have no known competing financial interests or personal relationships that could have appeared to influence the work reported in this paper.

Data availability

Data will be made available on request.

References

- Abbasi, H.R., Pourrahmani, H., Yavarinasab, A., Emadi, M.A., Hoofifar, M., 2019. Exergoeconomic optimization of a solar driven system with reverse osmosis desalination unit and phase change material thermal energy storages. *Energy Convers. Manag.* 199 (September), 112042. <https://doi.org/10.1016/j.enconman.2019.112042>.
- Abedinia, O., et al., 2024. Optimization of a syngas-fueled SOFC-based multigeneration system: enhanced performance with biomass and gasification agent selection. *Renew. Sustain. Energy Rev.* 199, 114460. <https://doi.org/10.1016/j.rser.2024.114460>.
- Abifarin, J.K., Abifarin, F.B., 2024. Carbon emission reduction and hydrogen production maximization from carbon emission-based hydrogen sources. *Environ. Sci. Pollut. Res.*, 0123456789 <https://doi.org/10.1007/s11356-024-34229-2>.
- Abifarin, J.K., Abifarin, F.B., Ofodu, J.C., 2024a. Lignin-hydrothermal fabrication of 3D hierarchical porous carbon for energy storage application. *Bioresour. Technol. Rep.* 26, 101883. <https://doi.org/10.1016/J.BITEB.2024.101883>.
- Abifarin, J.K., Torres, J.F., Lu, Y., 2024b. 2D materials for enabling hydrogen as an energy vector. *Nano Energy* 129, 109997. <https://doi.org/10.1016/J.NANOEN.2024.109997>.
- Abifarin, J.K., Oparanti, S.O., Abifarin, F.B., Obebe, E.O., 2025. Inhibitor additives to mitigate fossil fuel emissions and its potential role in promoting the energy transition in global cities. *Energy, Ecol. Environ.* 10 (4), 411–436. <https://doi.org/10.1007/s0974-025-00365-9>.
- Ahbabi Saray, J., Gharehghani, A., Hosseinzadeh, D., 2024. Towards sustainable energy carriers: a solar and wind-based systems for green liquid hydrogen and ammonia production. *Energy Convers. Manag.* 304, 118215. <https://doi.org/10.1016/j.enconman.2024.118215>.
- Ahmadi, S., Gharehghani, A., Soltani, M.M., Fakhari, A.H., 2022. Design and evaluation of renewable energies-based multi-generation system for hydrogen production, freshwater and cooling. *Renew. Energy* 198, 916–935. <https://doi.org/10.1016/J.RENENE.2022.08.081>.
- Alirahmi, S.M., Razmi, A.R., Arabkoohsar, A., 2021. Comprehensive assessment and multi-objective optimization of a green concept based on a combination of hydrogen and compressed air energy storage (CAES) systems. *Renew. Sustain. Energy Rev.* 142 (March), 110850. <https://doi.org/10.1016/j.rser.2021.110850>.
- Alovisio, A., Chacartegui, R., Ortiz, C., Valverde, J.M., Verda, V., 2017. Optimizing the CSP-calcium looping integration for thermochemical energy storage. *Energy Convers. Manag.* 136, 85–98. <https://doi.org/10.1016/J.ENCONMAN.2016.12.093>.
- Altayib, K., Dincer, I., 2024. Development of a large-scale integrated solar-biomass thermal facility for green production of useful outputs. *Energy* 313, 133741. <https://doi.org/10.1016/J.ENERGY.2024.133741>.
- Balali, A., Asadabadi, M.J.R., Mehrenjani, J.R., Gharehghani, A., Moghimi, M., 2023. Development and neural network optimization of a renewable-based system for hydrogen production and desalination. *Renew. Energy* 218, 119356. <https://doi.org/10.1016/J.RENENE.2023.119356>.
- Bauer, T., Steinmann, W.D., Laing, D., Tamme, R., 2012. Thermal energy storage materials and systems. In: Annual Review of Heat Transfer, vol. 15. Begell House Inc., pp. 131–177. <https://doi.org/10.1615/AnnualRevHeatTransfer.2012004651>.
- Boukelia, T.E., Bessaïh, R., Laouafi, A., 2025. A novel concentrating solar power plant design for power, cooling, and hydrogen production through integrated waste heat recovery system. *Int. J. Hydrogen Energy* 106, 295–304. <https://doi.org/10.1016/J.IJHYDENE.2025.01.376>.
- Ehyaei, M.A., Baloochzadeh, S., Ahmadi, A., Abanades, S., 2021. Energy, exergy, economic, exergoenvironmental, and environmental analyses of a multigeneration system to produce electricity, cooling, potable water, hydrogen and sodium-hypochlorite. *Desalination* 501 (December). <https://doi.org/10.1016/j.desal.2020.114902>.
- Eisavi, B., Ranjbar, F., Nami, H., Chitsaz, A., 2022. Low-carbon biomass-fueled integrated system for power, methane and methanol production. *Energy Convers. Manag.* 253 (September 2021), 115163. <https://doi.org/10.1016/j.enconman.2021.115163>.
- Farahmandfar, A., Gharehghani, A., Saray, J.A., 2025. Towards net-zero energy buildings: real-time monitoring, data-driven, and machine learning optimization. *Energy Convers. Manag.* 343, 120264. <https://doi.org/10.1016/J.ENERGY.2025.120264>.
- Fu, Y., Cai, L., Liu, C., Wu, M., Guan, Y., 2024. Thermodynamic and economic performance comparison of biomass gasification oxy-fuel combustion power plant in different gasifying atmospheres using advanced exergy and exergoeconomic approach. *Renew. Energy* 226 (February), 120290. <https://doi.org/10.1016/j.renene.2024.120290>.
- Ghorbani, A., Gharehghani, A., Saray, J.A., Andwari, A.M., Borhani, T.N., 2025. Integration of direct air capture with Allam cycle: innovative pathway in negative emission technologies. *Energy Convers. Manag.* 332 (February). <https://doi.org/10.1016/j.enconman.2025.119746>.
- Hai, T., et al., 2023. Deep learning optimization and techno-environmental analysis of a solar-driven multigeneration system for producing sustainable hydrogen and electricity: a case study of San Francisco. *Int. J. Hydrogen Energy* 48 (6), 2055–2074. <https://doi.org/10.1016/J.IJHYDENE.2022.09.301>.
- Hosseini Fakhari, A., Gharehghani, A., Mahdi Salahí, M., Mahmoudzadeh Andwari, A., 2024. RCCI combustion of ammonia in dual fuel engine with early injection of diesel fuel. *Fuel* 365, 131182. <https://doi.org/10.1016/J.FUEL.2024.131182>.
- Husaini, M.A., Darmanto, P.S., Juangsa, F.B., 2025. Integration of geothermal power plant, water treatment plant, AWE, and PEM electrolyzer for green hydrogen production: a techno-economic study. *Next Energy* 7, 100288. <https://doi.org/10.1016/J.NXENER.2025.100288>.
- Jabraelzadeh, A., Gharehghani, A., Ahbabí Saray, J., Mahmoodzadeh Andwari, A., Borhani, T.N., 2025. Techno-economic analysis of biogas upgrading through amine scrubbing: a comparative study of different single amines. *Fuel* 381 (July 2024). <https://doi.org/10.1016/J.FUEL.2024.133662>.
- Jalili, M., Ghazanfari Holagh, S., Chitsaz, A., Song, J., Markides, C.N., 2023. Electrolyzer cell-methanation/Sabatier reactors integration for power-to-gas energy storage: Thermo-economic analysis and multi-objective optimization. *Appl. Energy* 329, 120268. <https://doi.org/10.1016/J.APENERGY.2022.120268>.
- Jasim, D.J., Al-Rubaye, A.H., Kolsi, L., Khan, S.U., Aich, W., Marefatí, M., 2024. A fuel gas waste heat recovery-based multigeneration plant integrated with a LNG cold energy process, a water desalination unit, and a CO₂ separation process. *Helijon* 10 (4), e26692. <https://doi.org/10.1016/J.HELIYON.2024.E26692>.
- Karimi, M.H., Chitgar, N., Emadi, M.A., Ahmadi, P., Rosen, M.A., 2020. Performance assessment and optimization of a biomass-based solid oxide fuel cell and micro gas turbine system integrated with an organic Rankine cycle. *Int. J. Hydrogen Energy* 45 (11), 6262–6277. <https://doi.org/10.1016/J.IJHYDENE.2019.12.143>.
- Khodaei, E., Yari, M., Mohammad, S., 2023. Thermoeconomic optimization for a solar power generating system capable of storing energy by using calcium looping process. *Energy Convers. Manag.* 293 (June), 117403. <https://doi.org/10.1016/j.enconman.2023.117403>.
- Lak Kamari, M., Maleki, A., Daneshpour, R., Rosen, M.A., Pourfayaz, F., Alhuyi Nazari, M., 2023. Exergy, energy and environmental evaluation of a biomass-assisted integrated plant for multigeneration fed by various biomass sources. *Energy* 263, 125649. <https://doi.org/10.1016/J.ENERGY.2022.125649>.
- Manente, G., Lazzaretto, A., 2014. Innovative biomass to power conversion systems based on cascaded supercritical CO₂ Brayton cycles. *Biomass Bioenergy* 69, 155–168. <https://doi.org/10.1016/J.BIOMBIO.2014.07.016>.
- Mehrenjani, J.R., Gharehghani, A., Sangesaraki, A.G., 2022. Machine learning optimization of a novel geothermal driven system with LNG heat sink for hydrogen production and liquefaction. *Energy Convers. Manag.* 254 (November 2021), 115266. <https://doi.org/10.1016/j.enconman.2022.115266>.
- Mehrenjani, J.R., Shirzad, A., Adouli, A., Gharehghani, A., 2024. Data-driven optimization of two novel geothermal-powered systems integrating LNG regassification with thermoelectric generation for eco-friendly seawater desalination and data center cooling. *Energy*, 133846. <https://doi.org/10.1016/j.energy.2024.133846>.
- Mojaver, P., Khalilarya, S., Chitsaz, A., Jafarmadar, S., 2023. Plastic waste/chickpea straw-to-fuels and power through co-gasification in a novel zero-emission system by CO₂ capturing and utilization. *Fuel* 348 (April), 128490. <https://doi.org/10.1016/j.fuel.2023.128490>.
- Nami, H., Ranjbar, F., Yari, M., 2019. Methanol synthesis from renewable H₂ and captured CO₂ from S-Graz cycle – Energy, exergy, exergoeconomic and exergoenvironmental (4E) analysis. *Int. J. Hydrogen Energy* 44 (48), 26128–26147. <https://doi.org/10.1016/J.IJHYDENE.2019.08.079>.
- Ni, M., Leung, M.K.H., Leung, D.Y.C., 2008. Energy and exergy analysis of hydrogen production by a proton exchange membrane (PEM) electrolyzer plant. *Energy Convers. Manag.* 49 (10), 2748–2756. <https://doi.org/10.1016/j.enconman.2008.03.018>.

- Ohya, H., et al., 1997. Methanation of carbon dioxide by using membrane reactor integrated with water vapor permselective membrane and its analysis. *J. Memb. Sci.* 131 (1–2), 237–247. [https://doi.org/10.1016/S0376-7388\(97\)00055-0](https://doi.org/10.1016/S0376-7388(97)00055-0).
- Ortiz, C., Valverde, J.M., Chacartegui, R., Perez-Maqueda, L.A., Giménez, P., 2019. The Calcium-looping (CaCO₃/CaO) process for thermochemical energy storage in concentrating solar power plants. *Renew. Sustain. Energy Rev.* 113, 109252. <https://doi.org/10.1016/J.RSER.2019.109252>.
- Ortiz, C., Chacartegui, R., Valverde, J.M., Carro, A., Tejada, C., Valverde, J., 2021. Increasing the solar share in combined cycles through thermochemical energy storage. *Energy Convers. Manag.* 229, 113730. <https://doi.org/10.1016/J.ENCONMAN.2020.113730>.
- Romano, S.L., Sciuibba, E., Toro, C., 2014. Design and thermoeconomic evaluation of a waste plant with an integrated CO₂ chemical sequestration system for CH₄ production. *Int. Mech. Eng. Congr. Expo. - IMECE2014* 1–11. <https://doi.org/10.1115/IMECE2014-36873>.
- Sabbagh, M.A., Soltani, M., Rosen, M.A., 2024. A comprehensive 6E analysis of a novel multigeneration system powered by solar-biomass energies. *Energy* 297, 131209. <https://doi.org/10.1016/J.ENERGY.2024.131209>.
- Safder, U., Loy-Benitez, J., Yoo, C.K., 2024. Techno-economic assessment of a novel integrated multigeneration system to synthesize e-methanol and green hydrogen in a carbon-neutral context. *Energy* 290, 130104. <https://doi.org/10.1016/J.ENERGY.2023.130104>.
- Salah Kandezi, M., Mousavi Naeenian, S.M., 2022. Thermodynamic and economic analysis of a novel combination of the heliostat solar field with compressed air energy storage (CAES): a case study at San Francisco, USA. *J. Energy Storage* 49 (August 2021), 104111. <https://doi.org/10.1016/j.est.2022.104111>.
- Sánchez, D., Brenes, B.M., de Escalona, J.M.M., Chacartegui, R., 2012. Non-conventional combined cycle for intermediate temperature systems. *Arch. Thermodyn.* 33 (4), 23–40. <https://doi.org/10.1002/er>.
- Sharifishourabi, M., Dincer, I., Mohany, A., 2024. Advancing energy transition with novel biomass-solar based multigeneration energy system using hydrogen and storage options for sustainable cities. *Sustain. Cities Soc.* 108, 105457. <https://doi.org/10.1016/J.SCS.2024.105457>.
- Shokri, A., Shakibi, H., Azizi, S., Yari, M., Mahmoudi, S.M.S., 2024. Optimization of biomass-fueled multigeneration system using SOFC for electricity, hydrogen, and freshwater production. *Int. J. Hydrogen Energy* 88 (May), 1293–1320. <https://doi.org/10.1016/j.ijhydene.2024.09.161>.
- Su, W., 2025. Optimization and exergoeconomic analysis of a biomass-driven cogeneration system for power and cooling applications. *Appl. Therm. Eng.* 258 (PA), 124510. <https://doi.org/10.1016/j.applthermaleng.2024.124510>.
- Sun, K., et al., 2024. Thermodynamic feasibility evaluation of an innovative multigeneration system using biogas dry reforming integrated with a CCHP-desalination process. *Desalination* 580, 117526. <https://doi.org/10.1016/J.DESAL.2024.117526>.
- Tehrani, S.S.M., Taylor, R.A., 2016. Off-design simulation and performance of molten salt cavity receivers in solar tower plants under realistic operational modes and control strategies. *Appl. Energy* 179, 698–715. <https://doi.org/10.1016/j.apenergy.2016.07.032>.
- Toro, C., Sciuibba, E., 2018. Sabatier based power-to-gas system: heat exchange network design and thermoeconomic analysis. *Appl. Energy* 229, 1181–1190. <https://doi.org/10.1016/J.APENERGY.2018.08.036>.
- Wang, H., et al., 2023. Multi-criteria evaluation and optimization of a new multigeneration cycle based on solid oxide fuel cell and biomass fuel integrated with a thermoelectric generator, gas turbine, and methanation cycle. *Process Saf. Environ. Prot.* 170, 139–156. <https://doi.org/10.1016/J.PSEP.2022.11.087>.
- Wang, J., et al., 2024. A renewable multigeneration system based on biomass gasification and geothermal energy: Techno-economic analysis using neural network and grey wolf optimization. *J. Energy Storage* 104, 114519. <https://doi.org/10.1016/J.JEST.2024.114519>.
- Wang, Z., He, N., Chen, Q., Zhang, Y., Yao, L., 2025. Co-generation of methanol and electricity using integrated concentrated solar power, calcium looping, and methane bi-reforming: energy, exergy and economic analyses. *Energy Convers. Manag.* 327 (July 2024). <https://doi.org/10.1016/j.enconman.2025.119585>.
- Xu, H.J., et al., 2025. Progress on thermal storage technologies with high heat density in renewables and low carbon applications: latent and thermochemical energy storage. *Renew. Sustain. Energy Rev.* 215, 115587. <https://doi.org/10.1016/J.J.RSER.2025.115587>.
- Yan, X., Yao, K., Han, Y., Hou, J., Mao, X., Li, M., 2025. Proposal of a hybrid biomass/geothermal driven multigeneration system for methanol, power, and hydrogen production: a thermodynamic and economic assessment. *Energy* 324, 135954. <https://doi.org/10.1016/J.ENERGY.2025.135954>.
- Yang, K., et al., 2024. Exergy, exergoeconomic, and ergoenviromental analyses of novel solar- and biomass-driven trigeneration system integrated with organic Rankine cycle. *Energy* 301, 131605. <https://doi.org/10.1016/J.ENERGY.2024.131605>.
- Yao, A., Wu, J., 2025. Efficient biomass utilization for power, cooling, and hydrogen: a multi-generation approach with environmental and economic assessment. *Renew. Energy* 244 (January). <https://doi.org/10.1016/j.renene.2025.122645>.
- Yörükli, H.C., et al., 2025. A comprehensive review on biological methanation processes: from gaseous feedstocks to biomethane. *Energy Convers. Manag.* 341, 120075. <https://doi.org/10.1016/J.ENCONMAN.2025.120075>.
- Zainal, Z.A., Ali, R., Lean, C.H., Seetharamu, K.N., 2001. Prediction of performance of a downdraft gasifier using equilibrium modeling for different biomass materials. *Energy Convers. Manag.* 42 (12), 1499–1515. [https://doi.org/10.1016/S0196-8904\(00\)00078-9](https://doi.org/10.1016/S0196-8904(00)00078-9).
- Zhang, T., Sobhani, B., 2024. Multi-criteria assessment and optimization of a biomass-based cascade heat integration toward a novel multigeneration process: application of a MOPSO method. *Appl. Therm. Eng.* 240, 122254. <https://doi.org/10.1016/J.APPLTHERMALENG.2023.122254>.
- Zhang, J., et al., 2023. Thermodynamic analysis of a food waste plasma gasification-based multigeneration system with dehumidification and carbon capture. *J. Clean. Prod.* 402, 136844. <https://doi.org/10.1016/J.JCLEPRO.2023.136844>.
- Zhang, D., et al., 2025a. 3-E analysis of a hybrid multigeneration carbon-free process based on the integration of Allam-Z cycle and CO₂ electroreduction cell. *Renew. Energy* 241, 122237. <https://doi.org/10.1016/J.RENENE.2024.122237>.
- Zhang, Y., et al., 2025b. 4E (Energy, Exergy, Economic, Environment) analysis and optimization of a multigeneration system integrating two energy storage systems for remote islands. *Appl. Therm. Eng.* 273, 126523. <https://doi.org/10.1016/J.APPLTHERMALENG.2025.126523>.